Bachelor's degree in physics engineering

Bachelor's thesis

Design and construction of a 3D Helmholtz coil system for the ALBA magnetic measurements laboratory

by

Andrea del Carme Fontanet Valls

Director:
Dr. Jordi Marcos Ruzafa | ALBA Synchrotron

Co-director:
Dr. Jordi José Pont | UPC

June, 2019

Abstract

3D Hall probes designed and produced by ALBA Synchrotron are currently being used at ALBA magnetic measurements laboratory to carry out accurate magnetic characterization of magnets and insertion devices. In order to characterize the magnetic fields with great accuracy, it is essential to have measuring devices calibrated with a high degree of precision. In this thesis we present the design and construction of a system of 3D Helmholtz coils with the objective of generating a magnetic field in any direction in a controlled way. This system will be used to determine with detail the response of the 3D Hall probes when applying magnetic fields with different orientations. The system will generate magnetic fields of up to 50 G with an expected angular precision of 0.2 mrad.

Moltes gràcies a tota la gent que m'ha ajudat en l'elaboració d'aquest treball i especialment, a Jordi Marcos.

Contents

List of Figures

List of Tables

List of Symbols

N	Number of turns
R	Coil radius
I	Current
j	Current density
d	Conductor diameter
a_{cond}	Conductor cross section
h	Side of the square coil cross section
A	Coil cross section
μ_0	Vacuum permeability
B	Magnetic field
R_{el}	Electrical resistance
P_{el}	Electrical power
ρ_{Cu}	Copper electrical resistivity
c_{Cu}	Copper specific heat
h_c	Convective heat transfer coefficient
S	Surface area of the coil
f_c	Filling factor

1 Introduction

ALBA is a synchrotron light facility located in Cerdanyola del Vallès that came into operation in 2012. ALBA is managed by the Consortium for the Construction, Equipping and Exploitation of the Synchrotron Light Source (CELLS) and it is founded in equal parts by the Spanish and the Catalonian Administration.

This large scientific infrastructure is designed to produce synchrotron light, which allows the visualization of the atomic and molecular structure of matter as well as the study of its properties and therefore, it can be used practically in all scientific research areas. ALBA synchrotron has a perimeter of 270 meters which has 17 straight sections available for the installation of insertion devices and it currently has eight operational state-of-the-art beamlines.

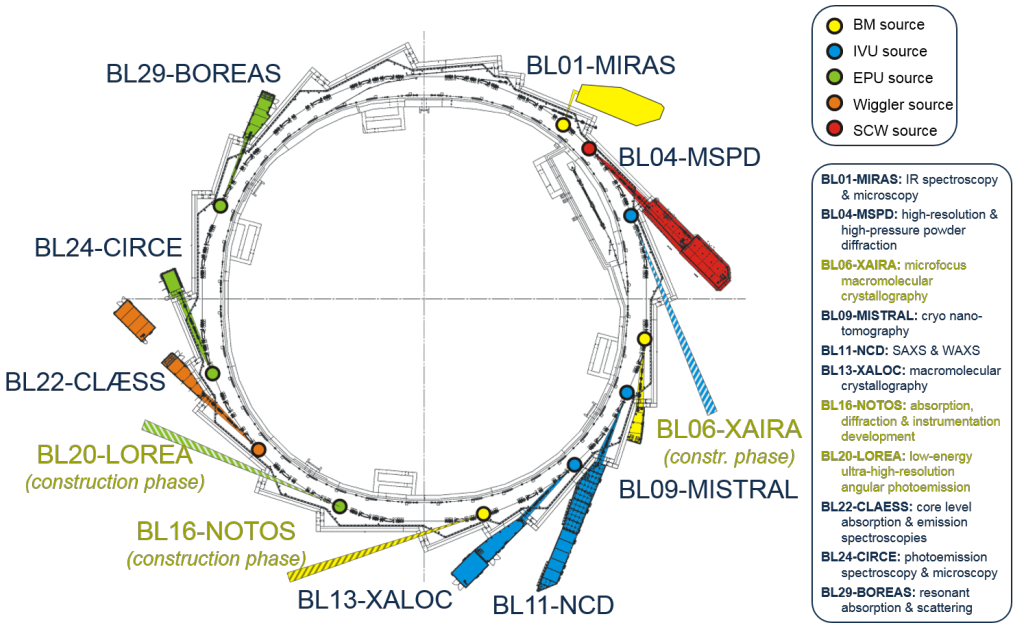

Figure 1.1: Schematic layout of ALBA synchrotron and the distribution of the different beamlines.

Synchrotron light is emitted by the electrons when they move at velocities near the speed of light in curvilinear trajectories. ALBA runs at an electron beam energy of 3 GeV, which is achieved by combining a linear accelerator (LINAC) and a low-emittance, full-energy booster placed in the same tunnel as the storage ring. ALBA

accelerators are equipped with different types of electromagnets (dipole magnets, quadrupole magnets, sextupole magnets) used to guide and focus the electrons along the trajectory. Finally, to provide the light beam with the characteristics that each beamline requires, insertion devices made of coils or made of permanent magnets are used.

Therefore, the role of magnetic fields in a synchrotron is very important and to have a precise characterization of them is a crucial factor. That's why the ALBA Synchrotron magnetic measurements laboratory has a great relevance within the complex and is where the magnetic characterization of magnets and insertion devices is carried out.

1.1 Motivation and brief description of the work carried out

In order to characterize the magnetic fields with great accuracy it is essential to have very well calibrated measuring devices. A 3D Hall probe designed and produced by ALBA is currently being used at ALBA magnetic measurements laboratory.

Figure 1.2: View of the ALBA magnetic measurement laboratory.

The Hall probe consists of three individual Hall effect sensors assembled in a quasi-orthogonal arrangement. During the calibration process of the 3D Hall probes, the angular deviations from ideal orthogonal arrangement are measured, and the obtained values are introduced in the algorithm that transforms the Hall voltage measured by the Hall sensors into 3D magnetic field components. The current calibration methodology has an accuracy of approximately 10 mrad.

So as to face the current challenges in magnetic measurements, it is necessary an increase in the accuracy of the determination of angular deviations of the 3D ALBA Hall probe. In this work we describe how we have carried out the design

and construction of a 3D Helmholtz coil system with a high mechanical accuracy allowing the achievement of an angular precision in the calibration of Hall effect probes of approximately 0.2 mrad.

To perform the design, a magnetostatic simulation code (RADIA) has been used to analyse the influence of the geometric and design parameters (coil radius, conductor diameter, number of turns, current) of a pair of Helmholtz coils over the merit figures of the system (intensity and homogeneity of the magnetic field generated, heating of the system). For the analysis of the thermal effects associated with power dissipation in coils, we have used finite element simulations made with the Siemens NX program.

Then, we have optimized the design of the three-dimensional coil system in order to achieve a compromise between the values of the different figures of merit. In addition, once the model has been defined, the possible errors in the manufacture and alignment of the coils on the characteristics of the generated magnetic field have been studied, and the tolerances required to achieve the quality of the desired field have been determined. After that, the set of drawings for its manufacture has been prepared.

To sum up, this bachelor's thesis arises from the need to have a system at ALBA magnetic measurements laboratory that allows us to generate a well defined magnetic field in order to calibrate 3D Hall probes with great accuracy. This system will consist of three orthogonal pairs of Helmholtz coils and, in the different sections of this work, the entire process of its design is detailed.

2 Theoretical fundamentals

2.1 1D Helmholtz coil

A Helmholtz coil pair consists of two equal parallel coaxial circular coils which are connected in series and separated by a distance equal to their common radius. This configuration is used to establish a known and nearly uniform magnetic field in a region surrounding the centre point of the axis between the two coils [1].

Our interest is in the calculation of the magnetic field B at the midpoint between the coils. First, we start calculating the magnetic field at a point on the axis of a circular current loop a distance x from the circular loop's centre.

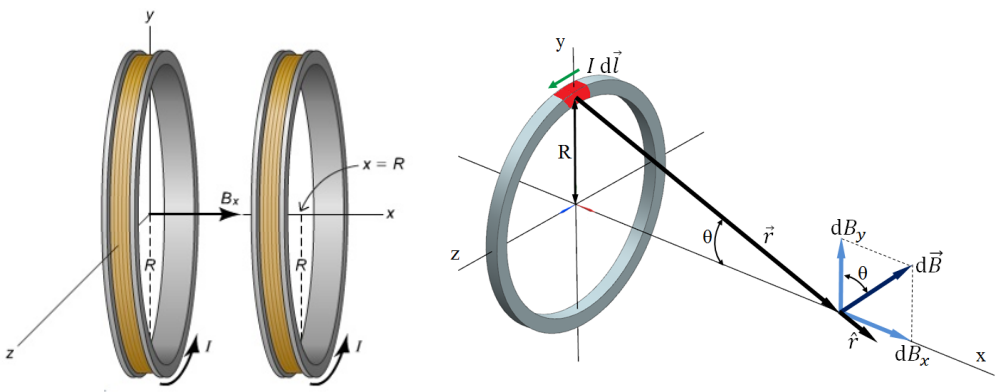

Figure 2.1: *Left*: Model of a 1D Helmholtz coil pair. *Right*: Geometry for calculating the magnetic field at a point on the axis of a circular current loop.

The **Biot-Savart law** states that the magnetic field $d\vec{B}$ produced by a current element $I\ d\vec{l}$ is given by

$$d\vec{B} = \frac{\mu_0}{4\pi}\frac{I\ d\vec{l} \times \hat{r}}{r^2} \tag{2.1}$$

Therefore, the magnitude for the on-axis field $d\vec{B}$ due to a single wire loop segment is

$$|d\vec{B}| = \frac{\mu_0}{4\pi}\frac{I\ |d\vec{l} \times \hat{r}|}{r^2} = \frac{\mu_0}{4\pi}\frac{I\ dl}{(x^2 + R^2)} \tag{2.2}$$

where we have used the facts that $r^2 = x^2 + R^2$ and that $d\vec{l}$ and $\hat{r}$ are perpendicular, so $|d\vec{l} \times \hat{r}| = dl$. μ_0 is the vacuum permeability ($4\pi \cdot 10^{-7}$ N/A^2).

When we sum around all the current elements in the loop, the components of $d\vec{B}$ perpendicular to the axis of the loop, such as $d\vec{B}_y$ in Fig. 2.1, sum zero, which leave only the component $d\vec{B}_x$ that is parallel to the axis. Thus,

$$dB_x = dB \sin\theta = \frac{\mu_0}{4\pi} \frac{I\ dl}{(x^2 + R^2)} \frac{R}{\sqrt{x^2 + R^2}} = \frac{\mu_0}{4\pi} \frac{IRdl}{(x^2 + R^2)^{3/2}} \tag{2.3}$$

To find the field due to the entire loop of current, we integrate dB_x around the loop and the magnetic field B_x results

$$B_x = \frac{\mu_0 I R^2}{2(x^2 + R^2)^{3/2}} \tag{2.4}$$

The Helmholtz coils consist of N turns of wire, so we must substitute I for NI in Eq. (2.4) to obtain the field for an N-turn coil:

$$B_x(x) = \frac{\mu_0 N I R^2}{2(x^2 + R^2)^{3/2}} \tag{2.5}$$

Moreover, in a Helmholtz coil, a point halfway between the two loops has an x value equal to $R/2$, so the field strength at that point is

$$B_x(R/2) = \frac{\mu_0 N I R^2}{2((R/2)^2 + R^2)^{3/2}} \tag{2.6}$$

Finally, we must take into account that there are two coils placed on the same axis (i.e., one coil is at $x = 0$ and the second coil is at $x = R$) and from symmetry, the field strength B_H at the midpoint is twice the single coil value (See Fig. 2.2):

$$B_H(R/2) = 2B_x(R/2) = \frac{8}{5\sqrt{5}} \frac{\mu_0 N I}{R} \tag{2.7}$$

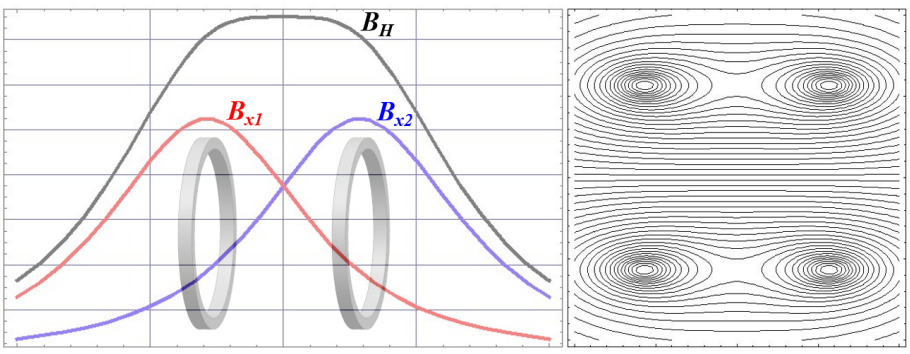

Figure 2.2: *Left*: Magnetic field generated by a 1D Helmholtz coil along the x axis, which is obtained by superimposing the two constituent fields. *Right*: Magnetic field lines for Helmholtz coils. Between the coils the lines are straight as a consequence of the uniformity of the field.

2.2 The Hall effect

The Hall effect is a galvanomagnetic phenomenon that produces, as a response, the appearance of a potential difference (Hall voltage) between the two edges of a conductor or a semiconductor strip through which is flowing a current density in presence of a magnetic field component perpendicular to the flow direction. The resulting Hall voltage is proportional to the magnetic field intensity and to the current and it is developed across the material in a direction perpendicular to both the current and to the magnetic field. Hall effect sensors are devices that exploit the Hall effect to measure the magnitude of a magnetic field. Thus, this phenomenon is an ideal magnetic field sensing technology.

2.2.1 Simplified approach of the Hall effect

In this section we describe the Hall effect in its simplest and classic form, where a long current-carrying strip is exposed to a magnetic field [2]. We consider a Hall effect sensor made of a thin strongly extrinsic n-type isotropic semiconductor (the majority carriers are electrons) with length L in the x direction, width w in the y direction and thickness t in the z direction. We assume a particle charge $e = -q$, a charge carrier number density n (i.e., number of carrier per unit volume) and the same velocity v_n for all the electrons (smooth drift approximation) when a current I flows in the longitudinal direction (See Fig. 2.3).

The current I is equal to the current density j times the cross sectional area of the conductor wt and j is the charge density $-nq$ times the velocity of the electron v_n. Therefore, I is given by

$$I = jwt = -nqv_n wt \tag{2.8}$$

When no magnetic field is applied, the electrons move in the longitudinal direction parallel to the longitudinal external electrical field E_e applied. The current density j is related to the electric field by Ohm's law:

$$j = \sigma E_e \tag{2.9}$$

where σ is the material conductivity.

As soon as the semiconductor is placed in a magnetic field perpendicular to the plane of the slab, the charge carriers experience a Lorentz force $-q\vec{v}_n \times \vec{B}$ that deflect them toward one edge of the strip. Consequently, there is an accumulation of charges along one side of the slab which creates a transverse electric field E_H that counteracts the force of the magnetic field.

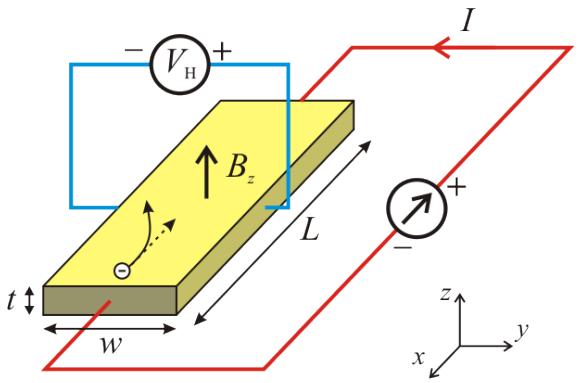

Figure 2.3: Diagram illustrating the Hall effect and governing parameters.

Equilibrium is reached when the magnetic force pushing the carriers aside and the reacting electric force pushing them back to the middle are balanced. At this point, electrons will again move in the longitudinal direction. Then, this equilibrium is expressed by

$$\vec{E}_H = -\vec{v}_n \times \vec{B} \tag{2.10}$$

where E_H is the Hall field, that can be expressed only as a function of the velocity of the electrons and of the applied magnetic field.

Moreover, a measurable transverse voltage V_H (Hall voltage) is produced between the two sides of the strip. This represents the most tangible effect associated with the Hall effect. V_H can be calculated along the width of the strip using

$$V_H = -\int_0^w \vec{E}_H \, \vec{dl} = -\frac{j}{nq} B_z w = -\frac{1}{nq}\frac{IB_z}{t} = \frac{R_H}{t} IB_z = SB_z \tag{2.11}$$

R_H is known as Hall coefficient, which depends on intrinsic parameters of the sensor's material, and it is given for the electrons by $R_H = -1/(nq) = -\mu_n/\sigma$, where μ_n is the electrical mobility of the electrons. B_z is the magnetic field component perpendicular to the sensor and S is the resulting magnetic sensitivity providing the proportionality factor between the field to be measured and the generated voltage.

In a real situation, however, there are several deviations from the ideal linear behaviour: the measured voltage is different from zero in the absence of a magnetic field (offset voltage), the Hall coefficient of the sensor's material depends on temperature and, as a result, also the sensitivity, and finally, the Hall voltage has an additional contribution from the magnetic field components within the plane of the sensor, which is known as planar Hall effect ($\propto B_x B_y$). Apart from that, there are nonlinearities and higher-order cross-terms too. Therefore, the Hall voltage in a real situation can be expressed as

$$V_H(B_x, B_y, B_z) = V_{offset} + S(T)B_z + c_p B_x B_y + o(B^2) \tag{2.12}$$

where c_p is the planar Hall coefficient and $o(B^2)$ refers to the contribution of the non-linear therms excluding the planar Hall effect [3].

If we want to reach good accuracy in the determination of the magnetic field, this deviations from ideal behaviour have to be properly taken into account. For this reason, calibration using a parametric model based on Eq. (2.12) is important.

2.3 Calibration of 3D Hall probes at ALBA

Calibration is necessary to reconstruct the magnetic field being measured from the output signal of the Hall probes. The calibration is the test during which known values of the magnetic field are applied to the Hall probe and the corresponding output reading is recorded.

Hall probes at ALBA consist of an inhouse PCB board with three quasi-orthogonally mounted uniaxial commercial Hall sensors situated on top of an aluminium profile arm [3]. They are soldered on the circuit board with a typical accuracy of $\pm 3^{\circ}$. We use gallium arsenide planar sensors of GH-series (GH-700 and GH-701 models) from FW Bell, with a magnetic sensitivity of $S \sim 1\,\mathrm{VT}^{-1}$ for a control current of 5 mA and a sensitive area with a diameter of 0.3 mm. The three sensors are powered in series using a high stability current supply. Keithley 2001 voltmeters are used to record the generated Hall voltages, with a resolution of $7\,{}^{1}/_{2}$ digits. Furthermore, to keep the temperature of the probe within $\pm 0.05^{\circ}$C, Pt-100 temperature sensor and a heater are also mounted on the circuit board of the Hall probes (See Fig. 2.5).

During the calibration process of the 3D Hall probes, the angular deviations from ideal orthogonal arrangement are measured, and the obtained values are introduced in the algorithm that transforms the Hall voltage measured by the Hall sensors into 3D magnetic field components. It is crucial to determine these angular misalignments in order to enable a precise reconstruction of the magnetic field.

As we have said before, in this process of calibration we have to model the response of the Hall probe to an external field. First, if we consider only one Hall effect sensor, the magnetic field components in the reference system of the Hall sensor are given by

$$(B_X, B_Y, B_Z) = (B\cos\Phi\sin\Theta, B\sin\Phi\sin\Theta, B\cos\Theta) \tag{2.13}$$

where Θ and Φ are the polar and azimuthal angles of the magnetic field relative to the Hall sensor [4].

Then, the response of the Hall sensor to the applied field has the following expression:

$$V(B,\Theta,\Phi,T) = \sum_{l=0}^{\infty}\sum_{m=-l}^{l} c_{lm}(B,T)B^{l}Y_{lm}(\Theta,\Phi) \tag{2.14}$$

where $Y_{lm}(\Theta,\Phi)$ are spherical harmonics. However, according to the work of Bergsma [5], only some of the terms c_{lm} have a significant contribution to the value of V.

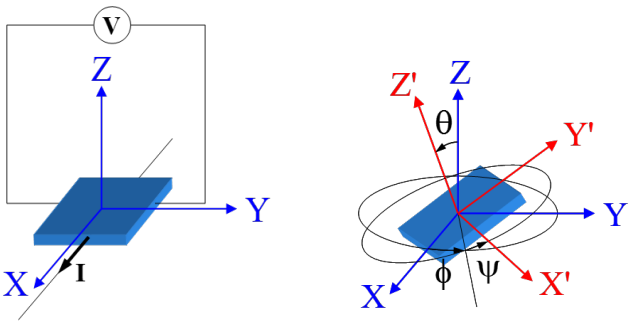

Figure 2.4: *Left*: Reference system of a Hall sensor. *Right*: Misalignment of the Hall sensor.

Furthermore, it shall be taken into account that the Hall sensors are not perfectly aligned with respect to the reference frame of the laboratory. We have the following relation:

$$\begin{pmatrix} B'_X \\ B'_Y \\ B'_Z \end{pmatrix} = \begin{pmatrix} \cos\psi & \sin\psi & 0 \\ -\sin\psi & \cos\psi & 0 \\ 0 & 0 & 1 \end{pmatrix} \begin{pmatrix} 1 & 0 & 0 \\ 0 & \cos\theta & \sin\theta \\ 0 & -\sin\theta & \cos\theta \end{pmatrix} \begin{pmatrix} \cos\phi & \sin\phi & 0 \\ -\sin\phi & \cos\phi & 0 \\ 0 & 0 & 1 \end{pmatrix} \begin{pmatrix} B_X \\ B_Y \\ B_Z \end{pmatrix} \tag{2.15}$$

where ψ, θ and ϕ are Euler angles defining the misalignment of the Hall sensor relative to the component of the magnetic field to be measured (See Fig. 2.4). As we have explained before, our objective in the process of calibration is to find the corresponding values of these angles.

Therefore, the response of the Hall sensor to an external field in terms of the laboratory frame components is

$$V\left[B'_X(B_X, B_Y, B_Z), B'_Y(B_X, B_Y, B_Z), B'_Z(B_X, B_Y, B_Z), T\right] \tag{2.16}$$

Eq. (2.16), based on Eq. (2.12), takes into account the offset voltage, nonlinearities, cross-terms between magnetic field components (planar Hall effect and higher-order terms) and the non-orthogonality between the three Hall sensors mounted on the circuit board. Since we have three Hall sensors, the Hall voltage generated on each sensor of the probe is thus expressed in terms of the three components of the external field.

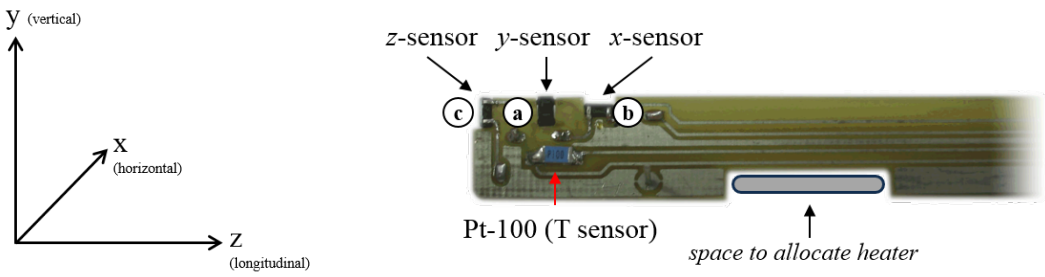

Figure 2.5: *Left:* Laboratory reference frame. *Right:* Diagram of a typical Hall probe used at ALBA.

vertical probe	ⓐ	$(X_a, Y_a, Z_a) \leftrightarrow (z, x, y)$	$V_a(B_x, \mathbf{B_y}, B_z, T)$
horizontal probe	ⓑ	$(X_b, Y_b, Z_b) \leftrightarrow (y, z, x)$	$V_b(\mathbf{B_x}, B_y, B_z, T)$
long. probe	ⓒ	$(X_c, Y_c, Z_c) \leftrightarrow (x, y, z)$	$V_c(B_x, B_y, \mathbf{B_z}, T)$

In the case of working with small values of B, only the offset voltage (c_{00}) and the linear terms will contribute significantly to the values of the voltages. Moreover, as the measurements will be done at constant temperature, the increment of temperature will be insignificant. Under these conditions, the expressions for the voltages result [4]:

$$\begin{aligned} V_a(B_x, B_y, B_z) &= c^a_{00} + c^a_{10} B^a_y \\ V_b(B_x, B_y, B_z) &= c^b_{00} + c^b_{10} B^b_x \\ V_c(B_x, B_y, B_z) &= c^c_{00} + c^c_{10} B^c_z \end{aligned} \tag{2.17}$$

$$ⓐ \begin{cases} B^a_y &= B_y \cos\theta_a + B_z \sin\phi_a \sin\theta_a - B_x \cos\phi_a \sin\theta_a \\ B^a_z &= B_y \sin\psi_a \sin\theta_a + B_z(\cos\phi_a \cos\psi_a - \sin\phi_a \sin\psi_a \cos\theta_a) + B_x(\sin\phi_a \cos\psi_a + \cos\phi_a \sin\psi_a \cos\theta_a) \\ B^a_x &= B_y \cos\psi_a \sin\theta_a - B_z(\cos\phi_a \sin\psi_a + \sin\phi_a \cos\psi_a \cos\theta_a) + B_x(\cos\phi_a \cos\psi_a \cos\theta_a - \sin\phi_a \sin\psi_a) \end{cases}$$

$$ⓑ \begin{cases} B^b_x &= B_x \cos\theta_b + B_y \sin\phi_b \sin\theta_b - B_z \cos\phi_b \sin\theta_b \\ B^b_y &= B_x \sin\psi_b \sin\theta_b + B_y(\cos\phi_b \cos\psi_b - \sin\phi_b \sin\psi_b \cos\theta_b) + B_z(\sin\phi_b \cos\psi_b + \cos\phi_b \sin\psi_b \cos\theta_b) \\ B^b_z &= B_x \cos\psi_b \sin\theta_b - B_y(\cos\phi_b \sin\psi_b + \sin\phi_b \cos\psi_b \cos\theta_b) + B_z(\cos\phi_b \cos\psi_b \cos\theta_b - \sin\phi_b \sin\psi_b) \end{cases}$$

$$ⓒ \begin{cases} B^c_z &= B_z \cos\theta_c + B_x \sin\phi_c \sin\theta_c - B_y \cos\phi_c \sin\theta_c \\ B^c_x &= B_z \sin\psi_c \sin\theta_c + B_x(\cos\phi_c \cos\psi_c - \sin\phi_c \sin\psi_c \cos\theta_c) + B_y(\sin\phi_c \cos\psi_c + \cos\phi_c \sin\psi_c \cos\theta_c) \\ B^c_y &= B_z \cos\psi_c \sin\theta_c - B_x(\cos\phi_c \sin\psi_c + \sin\phi_c \cos\psi_c \cos\theta_b) + B_y(\cos\phi_c \cos\psi_c \cos\theta_c - \sin\phi_c \sin\psi_c) \end{cases}$$

2.3.1 Calibration using 3D Helmholtz coil system

The misalignment angles between the Hall sensors are currently estimated at ALBA magnetic measurements laboratory by placing the probe inside a calibration dipole (Fig. 2.6) at a series of predefined orientations with the help of mechanized pieces. This calibration methodology has an accuracy of approximately 10 mrad.

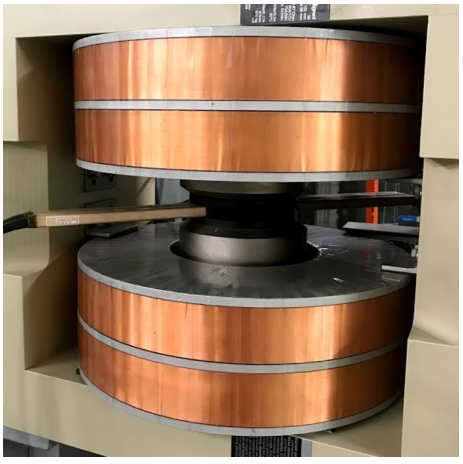

Figure 2.6: Calibration magnet.

Nowadays, it is necessary an increase in the accuracy of the determination of angular deviations of the 3D ALBA Hall probe. Nevertheless, because of the small gap dimension of the calibration magnet (15 mm), we cannot implement an accurate mechanical system providing a full control of the orientation of the Hall probe inside the magnetic field generated by the dipole. Thus, we have decided that we want to calibrate our 3D Hall probes with a 3D Helmholtz coil system with a high mechanical accuracy, that will allow us to generate a magnetic field with an arbitrary and well controlled orientation and it will also enable us the achievement of a better precision in the calibration of Hall effect probes. A similar system was designed and constructed at CERN [6].

Once we will have the coils that constitute de 3D Helmholtz coil system, we will have to determine the intensity necessary to generate a magnetic field B of a specific magnitude for each pair of coils. To do that, we will use a fluxgate magnetometer *Bartington Mag-01* ($|\mathrm{B}|<20\,\mathrm{G}$). As a result, we will obtain the coefficients that relate the intensity values that must be applied at each pair of coils.

Then, we will apply a sinusoidal function of intensities to each pair of coils. These functions will be out of phase from on pair to another in order to scan all the magnetic field values belonging to the surface of a sphere (of radius $|\mathrm{B}|$) situated at the centre of our system of coils. At each point of the sphere we will know the three components of the magnetic field (B_x, B_y, B_z), because there aren't ferromagnetic parts and thus, it's a linear system and the principle of superposition can be applied. While we apply the intensities, we have to place our Hall probes at the centre of the system of coils and the voltages measured by each sensor will be recorded.

Finally, we will apply least squares fitting using Eq. (2.17) in order to determine c_{00}, c_{10}, θ and ϕ parameters for each sensor. We can see that the angle ψ doesn't appear in Eq. (2.17) since it corresponds to an additional rotation around the principal axis of the sensor, and we will only obtain information if the applied magnetic field is large enough to consider a non negligible planar Hall effect.

All in all, after calibrating our Hall probes by means of the system of 3D Helmholtz coils, we expect to achieve an accuracy in the calibration of Hall effect probes of approximately 0.2 mrad.

3 | 3D Helmholtz coils design

3.1 Specifications of our design

We want to develop a model corresponding to a system of 3 dimension Helmholtz coils with the aim of generating a magnetic field of known direction and magnitude, and besides, this magnetic field must be homogeneous within 10^{-4} in a volume of 15x15x15 mm^3. It is worth saying that we have decided to impose our homogeneity requirement over a volume of 15x15x15 mm^3 because the sensors are mounted on the circuit board along a common line with a separation of 5.45 mm between them. The set of requirements that the system must fulfil is summarized in Tab. 3.1.

"Wish-list"	Specifications
3D Construction	3 pairs of coils
Minimum homogeneous magnetic field value to optimize the resolution for calibration	50 Gauss
Same field strength for all three axes	Needs to compensate with coil size and number of turns
Largest possible homogeneous field size (Homogeneity zone)	15x15x15 mm^3
Tolerance in the homogeneity of the magnetic field	$\sim 10^{-4}$, which is the same as, $\sim 0.01\%$
Cooling	Air cooling
Maximum system heating	20 °C
Magnetic field orthogonality	0.2 mrad

Table 3.1: 3D Helmholtz system specifications.

Thus, the model has to consider and establish the following aspects:

a) General dimensions of the system to guarantee the specified field homogeneity in its central zone.

b) Determination of the maximum field that can be generated taking into account the thermal dissipation of the coils.

c) Mechanical alignment tolerances of the different coils in order to achieve the accuracy required in the alignment of the generated magnetic field.

3.2 Design parameters

The magnetic field strength in a Helmholtz coil can be calculated by the expression

$$B = \left(\frac{4}{5}\right)^{\frac{3}{2}} \mu_0 \frac{NI}{R}$$

as we have deduced in Eq. (2.7). Therefore, the parameters that must be determined to achieve the desired magnetic field are the current (I), the number of turns (N) and the radius of the coil (R).

In addition, as we have specified in Tab. 3.1, another factor to take into account is the cooling of the coils, since they are heated as a consequence of the dissipated electrical power by Joule's effect. This fact can lead to mechanical distortions of the system and it can seriously damage the coil insulation and cause short circuits between the coil conductor and the surrounding equipment that is used.

We are interested in **air cooling** so as to avoid increasing the complexity of the whole system. Air cooling is a combination of natural convection, radiation and heat conduction, and it depends on coil geometry, coil surface (roughness, material, colour), thermal contact to the surrounding materials, etc. This type of cooling is possible when working with low current densities and, as a rule of thumb, the maximum current density that must be used for voluminous coils must not exceed $1\,\mathrm{A/mm^2}$ and, for the case of small coils and with smaller cross section, current density can be higher but below $2\,\mathrm{A/mm^2}$ ($1 \leq j \leq 2\ \mathrm{A/mm^2}$) [7].

The current density j in [A/m^2] is defined as follows:

$$j = \frac{N\ I}{f_c\ A} = \frac{I}{a_{cond}} \qquad \left(f_c = \frac{\text{net conductor area}}{\text{coil cross section}}\right) \tag{3.1}$$

where a_{cond} is the conductor cross section in [m^2], A corresponds to the coil cross section in [m^2] and f_c is a dimensionless geometric factor known as 'filling factor'.

The filling factor is the ratio of the area of electrical conductors to the provided winding space (coil cross section). The value of f_c varies depending on the winding precision, the thickness of the insulating material and the conductor cross section. We consider a circular cross section copper conductor and, owing to the fact that a round wire will create air gaps that are not electrically used, the fill factor will be smaller than one. The typical f_c value used for round conductors is 0.63 [7].

The total dissipated power for each coil is calculated by:

$$P_{el} = I^2 \cdot R_{el} \tag{3.2}$$

where R_{el} is the electrical resistance.

$$R_{el} = \rho_{Cu}\frac{l}{a_{cond}} = \rho_{Cu}\frac{N2\pi R}{\pi d^2/4} = \rho_{Cu}\frac{8NR}{d^2} \tag{3.3}$$

ρ_{Cu} is the electrical resistivity of the copper ($1.68 \cdot 10^{-18}\,\Omega\cdot$m) and d the diameter of the conductor.

In the following sections we detail the simulations done in order to determine the design parameters of our system of 3D Helmholtz coils.

3.3 Simulations with RADIA

RADIA is a fast multiplatform software dedicated to 3D magnetostatics computation [8]. We use this simulation code to calculate the magnetic field generated by the distribution of the 3 dimension Helmholtz coils that we want to design. Initially, we wrote a code where I, R, N and d were used as input parameters. The fact of having so many variables without a specific constraint made it difficult to determine the optimum configuration of the system.

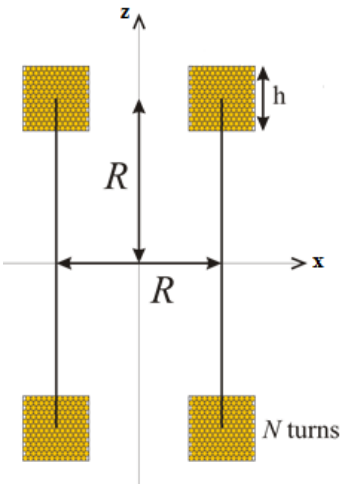

Figure 3.1: Diagram of the cross section of a Helmholtz pair generating a magnetic field along the x axis.

To better interpret the behaviour of the whole system and simplify the initial model, we start considering only a two-coil Helmholtz pair with one turn ($N = 1$) and perpendicular to x axis. Moreover, we just define the radius and the coil section as variables to see how the magnetic field strength and the tolerance in the homogeneity of the magnetic field change as functions of these two input parameters. It is worth saying that to carry out these first calculations, we consider an intensity of 20 A, which corresponds to the maximum current that the power supply of our laboratory can provide, and also that the coil section is square. Therefore, we calculate j dividing the intensity by the coil section. By the moment, we don't take into account f_c.

In order to calculate the tolerance in the homogeneity of the magnetic field provided by a pair of Helmholtz coils over a volume of 15x15x15 mm^3, the magnetic field between the two parallel coils is calculated at different points from -7.5 to 7.5 mm for each one of the coordinates. The distance between two consecutive points is called m. Therefore, we calculate the field along a distance of 15 mm and consequently, we obtain the magnetic field in $(15/m + 1)^3$ points within the volume 15x15x15 mm^3. Once the field is obtained, the module of each one of the field vectors is calculated. Then, the tolerance is the error percentage between the maximum value and the minimum value of the modulus of the magnetic field.

$$\text{Tolerance [\%]} = \frac{B_{max} - B_{min}}{B_{max}} \cdot 100 \tag{3.4}$$

Then, the field at the midpoint between the coils and the tolerance are calculated for different values of R and they are represented as functions of h/R (See Fig. 3.2), where h is one of the sides of the square coil section (See Fig. 3.1). The values corresponding to the coil section range from 10 mm^2 to 1060 mm^2 with a separation between points of 10 mm^2.

We also verify that the fact of considering more or less points when calculating the magnetic field in a volume 15x15x15 mm^3 is not critical for determining the value of the tolerance, as we can see in Tab. 3.2.

m	Minimum tolerance [%]	h/R
0.5	0.042609	0.176777
1.5	0.042609	0.176777
3	0.040461	0.176777

Table 3.2: Minimum value of the tolerance and the corresponding h/R for a specific value of m. In this case, R is equal to 80 mm.

For this reason, we decide that, for each one of the coordinates, we will calculate the magnetic field from -7.5 to 7.5 mm with a distance between consecutive points of 1.5 mm ($m = 1.5$ mm). Thus, the magnetic field is evaluated in $11^3 = 1331$ different points pertaining to the volume of 15x15x15 mm^3 in order to calculate the tolerance.

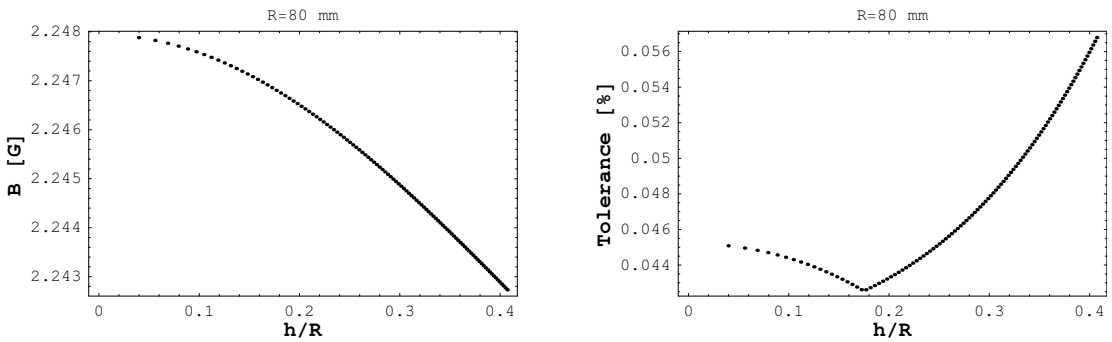

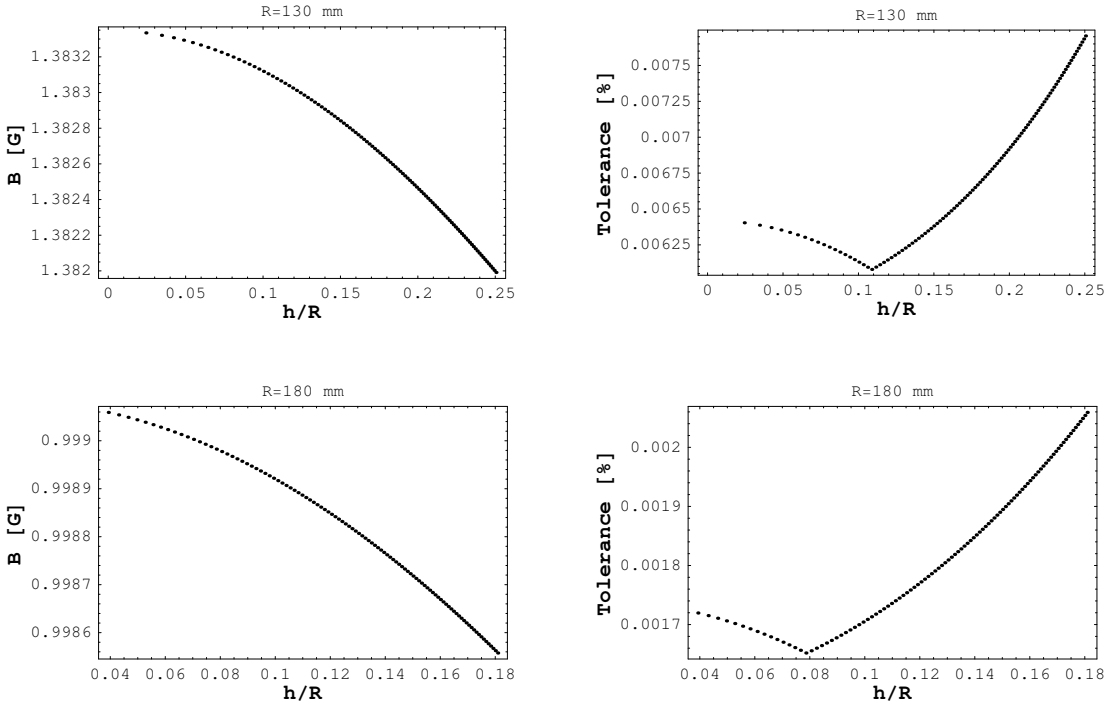

Figure 3.2: Magnetic field calculated at the midpoint between coils and tolerance as functions of h/R for different values of R.

As expected, the magnetic field is inversely proportional to the coil radius. With regard to the tolerance, it is also inversely proportional to the coil radius. The larger the radius, the better the volume of homogeneity. However, given a certain radius (R), as the section increases, the tolerance decreases but, at a specific point, it begins to increase as the section increases (See Fig. 3.2). Therefore, there is an optimum point where the tolerance is minimal, from which we can infer which is the most appropriate section value. Tab. 3.3 shows the magnetic field and section values corresponding to the point of minimum tolerance. However, the effect of changing the coil section on the field and the tolerance is much smaller than the effect of changing the coil radius.

R [mm]	Minimum tolerance [%]	h/R	Coil section [mm^2]	B [G]
80	0.042609	0.176777	200	2.24681
130	0.00607903	0.108786	200	1.38308
180	0.00165188	0.0785674	200	0.998983

Table 3.3: Coil section corresponding to the point of minimum tolerance for different values of R and the resulting magnetic field at the midpoint between coils.

We realise that the optimum coil section value is the same for any R value (Tab. 3.3). For this reason, we decide to prove how this optimal coil section varies as a function of the dimension variable s of the volume chosen where we calculate the magnetic field. Then, the volume where the magnetic field is calculated is $2s$x$2s$x$2s$ mm^3.

	s [mm]				
R [mm]	**4.5**	**6**	**7.5**	**9**	**10.5**
80	70	130	200	280	370
130	70	130	200	290	390
180	70	130	200	290	390

Table 3.4: Optimum coil section values for different values of s and for the three cases of R considered.

Fig. 3.3 shows the relation between the optimal value of h (h_{op}) and s for different values of R. This dependence is linear and in all cases the intercept is close to zero and the value of the slope is approximately 1.8.

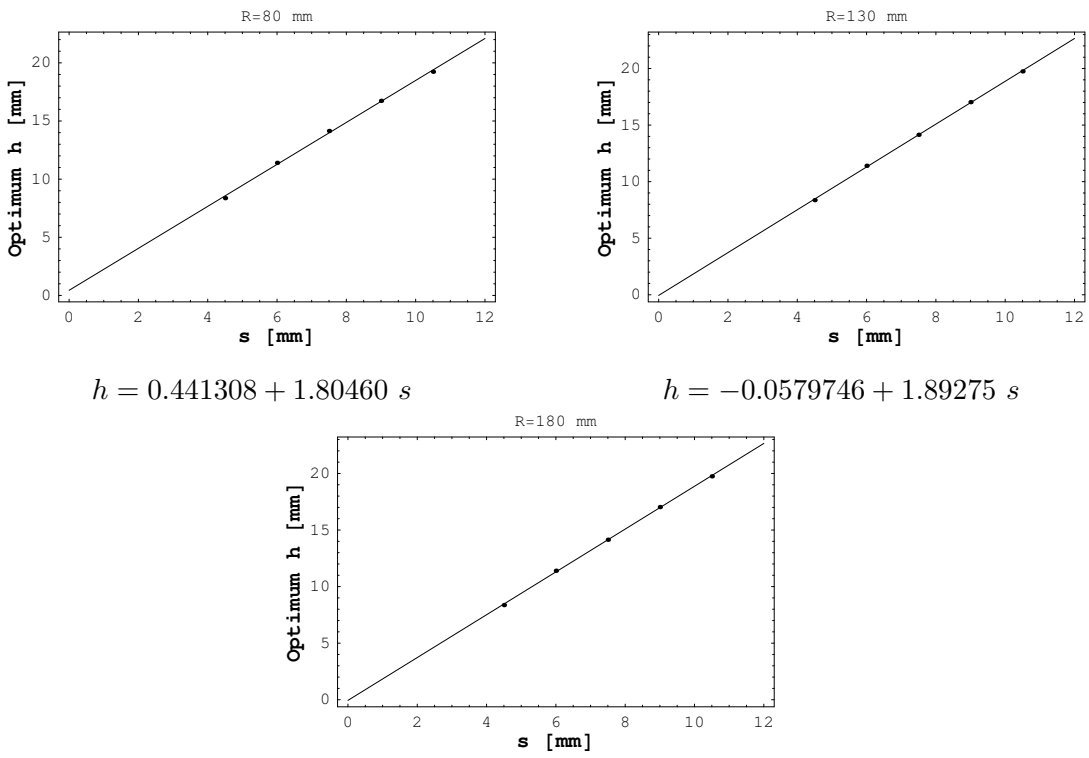

$h = 0.441308 + 1.80460\ s$

$h = -0.0579746 + 1.89275\ s$

$h = -0.0579746 + 1.89275\ s$

Figure 3.3: Optimum h as a function of s for different values of R. The straight line that better fits the points found with the simulation is also shown.

With the purpose of finding an explanation for the tolerance behaviour, we check if the points where B_x is maximum and minimum change for different section values, since we observe that the tolerance, which is a function of B, changes its tendency at a certain value of h. We use B_x instead of the modulus of B because both results are almost the same given the small values of B_y and B_z, that are nearly zero. Using RADIA simulations and taking $s = 7.5\,\mathrm{mm}$, we determine that the maximum is always located in the coordinate point (7.5, 7.5, 7.5). On the contrary, there is a certain section where the minimum change from the point (0, 7.5, 7.5) to (7.5, 0, 0). This section corresponds to the optimal section ($\sim$200 mm^2 when $s = 7.5\,\mathrm{mm}$), where the change in the trend of the curve can be appreciated when representing the tolerance vs. h/R (Fig. 3.2). We can find the explanation to this fact if we consider the analytical expressions of the magnetic field calculated near the centre of Helmholtz coils with a specific geometry and coil section.

3.4 Analytical expressions

If we consider ideal Helmholtz coils with square section (h^2) and perpendicular to x axis, the analytical expression of the magnetic field B at an off-axis point (x,y) near the centre of the Helmholtz coils is the following [9]:

$$B_x(x,y) = \frac{8\mu_0 NI}{5\sqrt{5}R}\left[1 - \frac{h^2}{60R^2} + F_{cx} + \frac{2x^2 - y^2}{125R^2}F_{2x} - \frac{18}{125R^4}(8x^4 - 24x^2y^2 + 3y^4) + ...\right] \tag{3.5a}$$

$$B_y(x,y) = \frac{8\mu_0 NI}{5\sqrt{5}R}\left[\frac{xy}{125R^2}F_{2y} + \frac{xy}{125R^4}(288x^2 - 216y^2) + ...\right] \tag{3.5b}$$

where $B_x(x,y)$ and $B_y(x,y)$ are, respectively, the axial and radial components (cylindrical coordinates) of the magnetic field and F_{cx}, F_{2x} and F_{2y} are defined as,

$$F_{cx} = \frac{31h^4}{1875R^4} \qquad F_{2x} = -\frac{5h^2}{R^2} \qquad F_{2y} = \frac{10h^2}{R^2} \tag{3.5c}$$

The model that has been used takes into account several geometrical parameters of the coils, such as their section, the separation between coils and their radius. It is worth saying that, as we work with ideal Helmholtz coils, the separation between coils is equal to the radius of one coil (R). In addition, it is necessary to keep in mind that the model described by Eq. (3.5) assumes that the current flows uniformly within the entire cross-sectional area h of the coil.

We have decided to work on plane $z = 0$, where the z component of the field is zero. Moreover, we have checked that the value of B_y is very small and it barely varies and therefore, to make the analytical study, instead of taking into account the module of B, we have only considered the B_x component. In Fig. 3.4, we have verified using the analytical expressions that the B_x component of the magnetic field as a function of the coil section (Eq. (3.5a)) behaves in the same way as with the RADIA function.

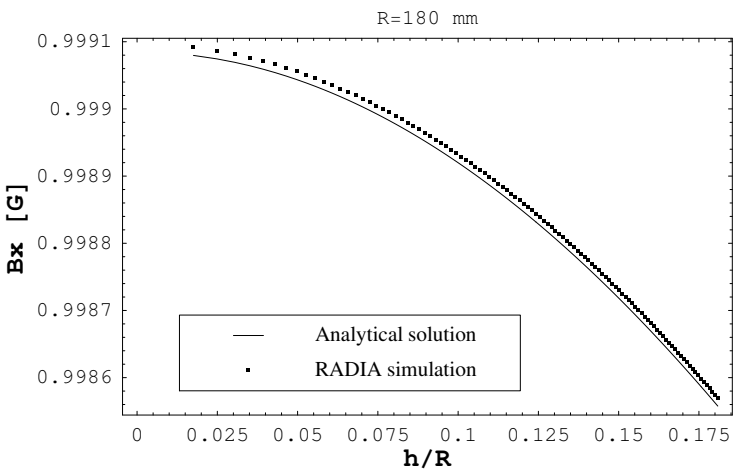

Figure 3.4: B_x calculated at the midpoint between coils using the analytical expression and the RADIA function. In this case, R is equal to 180 mm.

From the RADIA simulations, we know that the points where the magnetic field is minimum and maximum. The point where the magnetic field is maximum is $(s,\sqrt{2}s)$ and it is minimum at points $(0,\sqrt{2}s)$ and $(s,0)$ in cylindrical coordinates. Fig. 3.5 shows where these points are situated.

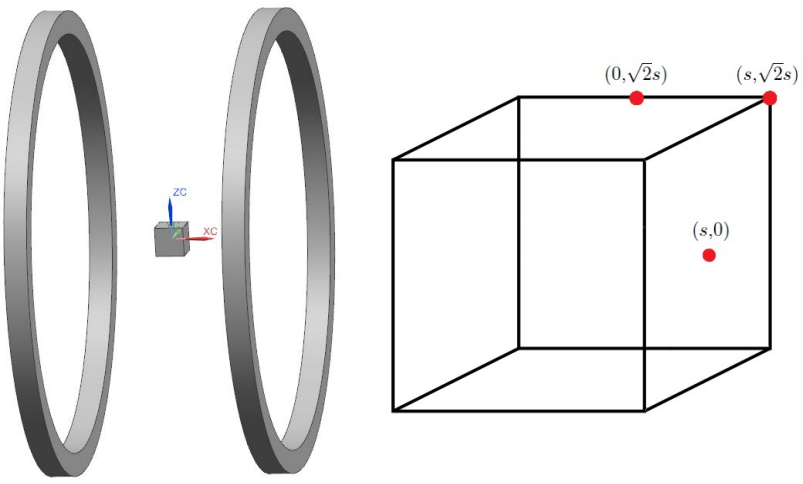

Figure 3.5: Volume between coils where we calculate the magnetic field. Red points show the coordinates where the field is maximum and minimum.

Using Eq. (3.5a), we can represent the magnetic field on the plane xy to see its behaviour and to prove again that the maximum and minimum points are where we have indicated before, depending on the value of h. To obtain the contour plots, we take, as an example, $I = 0.2\,\mathrm{A}$, $N = 1100$, $R = 115\,\mathrm{mm}$ and two different values of h. Since we have proved before that $h_{op} \sim \sqrt{200}\,\mathrm{mm} = 14\,\mathrm{mm}$, we choose $h_1 = 5\,\mathrm{mm}$

and $h_2 = 20\,\text{mm}$. Fig. 3.6 clearly shows that for any value of h, the maximum of the magnetic field is situated at $(s, \sqrt{2}s)$. By the contrary, for values of h smaller than h_{op} ($h_1 < h_{op}$) the minimum value of the magnetic field is at point $(0, \sqrt{2}s)$ and for the case $h_2 > h_{op}$ the minimum is at point $(s, 0)$. Moreover, a symmetrical magnetic field distribution with respect to zero is observed.

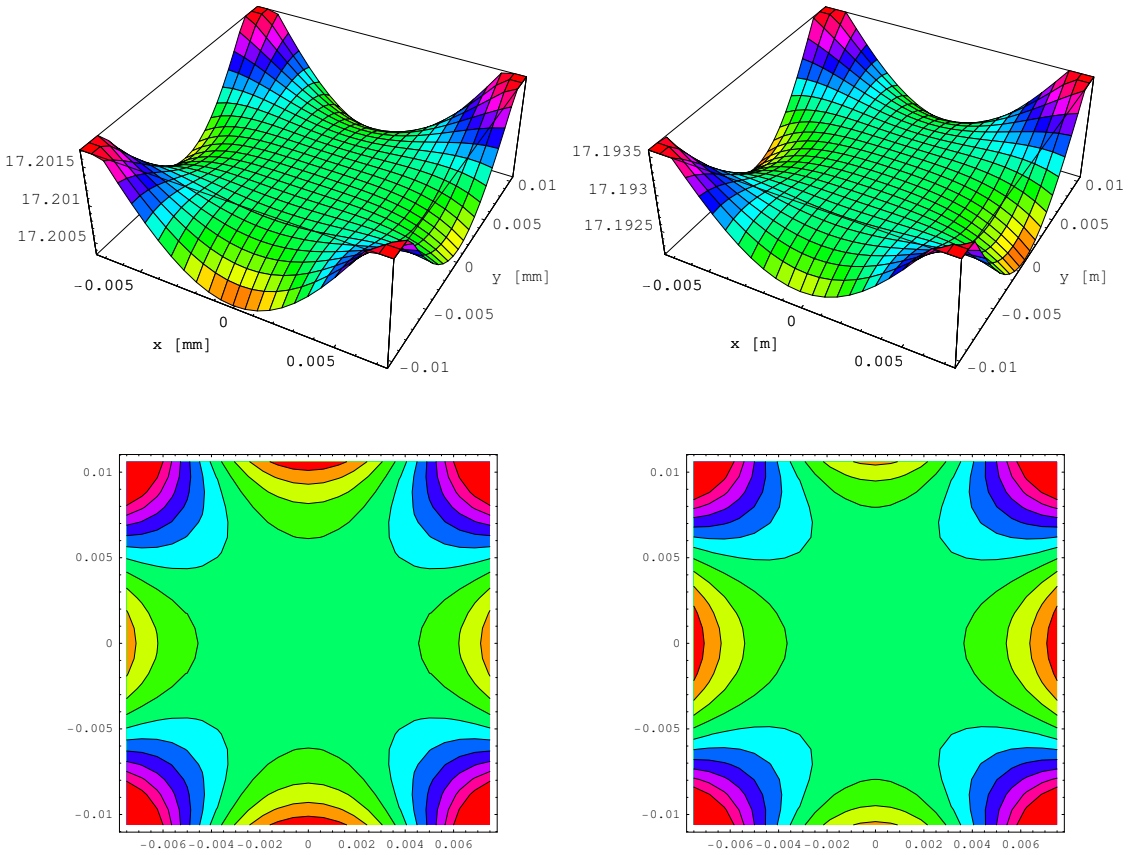

Figure 3.6: Contour plots of the magnetic field on the plane xy when considering $h_1 = 5\,\text{mm}$ (*left*) and $h_2 = 20\,\text{mm}$ (*right*).

We calculate the maximum value and the minimum values of B_x replacing in Eq.(3.5a) the coordinates of the maximum and of the two minimum points.

$$B_{x_{max}} = B_x(s, \sqrt{2}s) = \frac{8I\mu_0 N\left(1 + \frac{31h^4}{1875R^4} - \frac{h^2}{60R^2} + \frac{504s^4}{125R^4}\right)}{5\sqrt{5}R} \tag{3.6a}$$

$$B_{x_{min\ 1}} = B_x(0, \sqrt{2}s) = \frac{8I\mu_0 N\left(1 + \frac{31h^4}{1875R^4} - \frac{h^2}{60R^2} + \frac{2h^2s^2}{25R^4} - \frac{216s^4}{125R^4}\right)}{5\sqrt{5}R} \tag{3.6b}$$

$$B_{x_{min\ 2}} = B_x(s, 0) = \frac{8I\mu_0 N\left(1 + \frac{31h^4}{1875R^4} - \frac{h^2}{60R^2} - \frac{2h^2s^2}{25R^4} - \frac{144s^4}{125R^4}\right)}{5\sqrt{5}R} \tag{3.6c}$$

We equate Eq. (3.6b) and Eq. (3.6c) and, solving for h, we find that the optimal coil section value is $\mathbf{h_{op} = 1.89737 \cdot s\ mm}$. Therefore, the optimal section is proportional to the dimension s of the volume where we calculate B. It is worth saying that this value of h_{op} coincides with the slope of the straight lines of Fig. 3.3 and that $h_{op}^2 = 202.5\,\mathrm{mm}^2$ is approximately the value specified at Tab. 3.4 for the case of $s = 7.5\,\mathrm{mm}$.

If we calculate the tolerance with the expressions of the minimum field calculated at point (s,0) (Eq. (3.6c)) and the maximum field (Eq. (3.6a)) the analytical formula of the tolerance depends basically on R and it is very weakly dependent on h and s.

$$\begin{aligned} \text{Tolerance [\%]} &= \frac{B_{x_{max}} - B_{x_{min\ 2}}}{B_{x_{max}}} \cdot 100 \\ &= \frac{12000(5h^2s^2 + 324s^4)}{124h^4 - 125h^2R^2 + 7500R^4 + 30240s^4} \end{aligned} \tag{3.7}$$

In order to find R corresponding to a tolerance of 0.01%, we consider the optimal section value (h_{op}) and $s = 7.5\,\mathrm{mm}$. If we replace these values in Eq. (3.7), we find out a numerical expression providing an estimation of the tolerance as a function of R (in [mm]):

$$\text{Tolerance [\%]} = \frac{1.73138 \cdot 10^6}{13435.5 - 3.375R^2 + R^4} \tag{3.8}$$

Finally, solving Eq. (3.8) in order to achieve a tolerance of 0.01%, the result we get is that the radius of the coils must be at least $\boldsymbol{R = 115\,\mathrm{mm}}$.

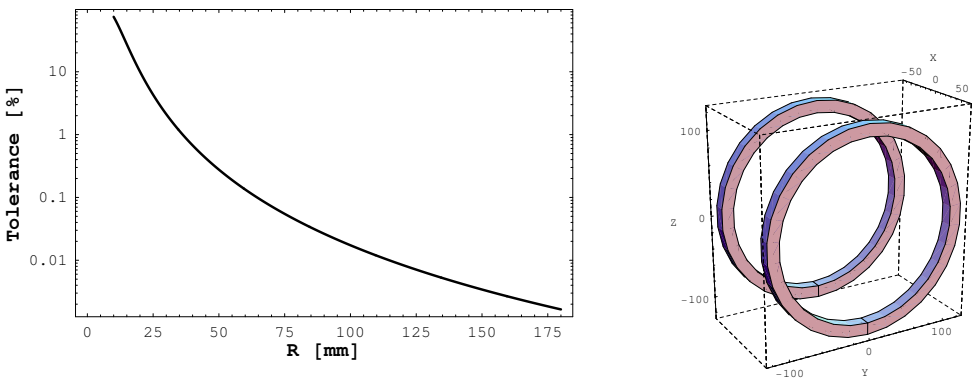

Figure 3.7: Tolerance vs. R and drawing of the Helmholtz coils perpendicular to x axis.

Furthermore, we know that air cooling is possible when working with current densities between $1\,\mathrm{A/mm}^2$ and $2\,\mathrm{A/mm}^2$. We take $j = 1.5\,\mathrm{A/mm}^2$ to calculate the intensity that must flow within the conductor with a specific section d without exceeding the above j value, knowing that $I = j \cdot a_{cond}$. Results are listed in Tab. 3.5.

d [mm]	I [A]
0.1	0.011781
0.2	0.0471239
0.3	0.106029
0.4	0.188496
0.5	0.294524
0.6	0.424115
0.7	0.577268
0.8	0.753982
0.9	0.954259
1.0	1.17810
1.1	1.42550
1.2	1.69646
1.3	1.99098
1.4	2.30907
1.5	2.65072

Table 3.5: Conductor diameter values (d) and the corresponding intensity (I) for a current density (j) of 1.5 A/mm^2.

To make a first estimation, we choose a conductor of $d = 1.5\,\text{mm}$, since working with a conductor diameter not too small will facilitate the arrangement of the successive layers during the winding process. In addition, with a diameter of 1.5 mm, the number of turns will remain in the range of a few hundred. Then, with $h_{op} = 1.89737 \cdot 7.5\,\text{mm}$, $f_c = 0.63$, the resulting $R = 114.714\,\text{mm}$, $j = 1.5\,\text{A/mm}^2$, $d = 1.5\,\text{mm}$ and the corresponding $I = 2.650\,72\,\text{A}$, we can calculate N with Eq. (3.1) and we obtain $N = 72\,\text{turns}$. Using these data, we calculate the magnetic field and the tolerance with RADIA:

$$B = 14.9961\ \text{G}$$
$$\text{Tolerance} = 0.0100424\ \%$$

This result does not satisfy the initial wish-list regarding the result of the magnetic field, since we do not achieve the minimum desired value of 50 G. However, we have proved that the tolerance is dominated by R and that h barely affects its result. So, we conclude that we can increase h ($>h_{op}$) to increase N and consequently increase B. With these changes, the tolerance will have a value close to 0.01% as well.

Apart from accomplishing the requirement of the magnetic field strength and the tolerance, we aim at keeping the heating of the system due to the power dissipation at a reasonable level ($<$20°C). Thus, the coil's characteristics (d, N, etc.) and I, which will determine the maximum magnetic field attainable by the system, will be dictated by thermal considerations. We will analyse coil's heating so as to find an expression for the increase of the coil's temperature as a function of the time and we will simulate this behaviour using Siemens NX software. Then, we will be able to use Multi-objective Optimization in order to find the most suitable solution.

3.5 Thermal analysis

The temperature of a coil increases as a consequence of the dissipated electrical power by Joule's effect. As indicated in Tab. 3.1, we have decided to use air cooled coils so as to avoid increasing the complexity of the system. In this section we analyse how a coil is heated with the objective of calculating the maximum temperature that the coil can reach. To do that, we have taken into account a simplified model in which the coil is approximated by a copper solid form with the same section dimensions.

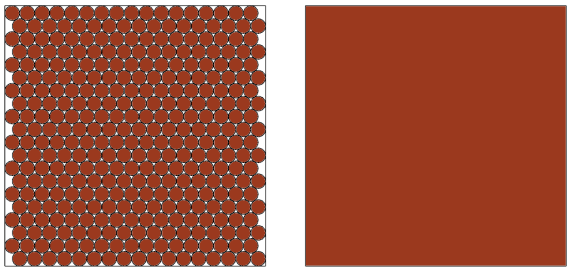

Figure 3.8: *Left*: Real view of the coil section. *Right*: Coil section view of the simplified model.

We have considered that the electrical power P_{el} dissipated on each coil is equal to the increase rate of internal energy plus the rate of heat loss through the surface. Then, P_{el} results:

$$P_{el} = \frac{dU}{dt} + \oint j_t \cdot ds = mc_{Cu}\frac{dT}{dt} + h_c S \Delta T \tag{3.9}$$

where c_{Cu} is the copper specific heat (390 $\mathrm{Jkg^{-1}K^{-1}}$), h_c is the convective heat transfer coefficient, S the surface area of the coil and ΔT is the difference in temperature between the solid surface and the surrounding fluid area (assumed to be at 20°C).

The second therm of Eq. (3.9) refers to the energy exchange through convection and results from the integration of heat flux (j_t) over the surface S of the coil. Convection cooling is assumed to be described by **Newton's law of cooling**. This law is a discrete analogue of Fourier's law of heat conduction and states that the rate of heat loss of a body is proportional to the difference in temperatures between the body and its surroundings. It should be noted that Newton's law applies when h_c is independent of the temperature and, although in classical natural convective heat transfer h_c is dependent on the temperature, the above law does approximate reality when the temperature changes are relatively small.

In stationary state, dU/dt tends to 0 since the internal energy is constant and only the second term in Eq. (3.9) remains. As a result, $P_{el} = h_c S \Delta T$, from which we can isolate ΔT. Knowing that $P_{el} = I^2 R_{el}$, we obtain that the maximum increase in temperature is

$$\Delta T_{max} = \frac{I^2 R_{el}}{h_c S} \qquad \text{being} \qquad S = 8\pi h R \tag{3.10}$$

Eq. (3.10) can also be written in terms of the parameters of the coil using Eq. (3.3) and $d = 2h\sqrt{\frac{f_c}{\pi N}}$:

$$\Delta T_{max} = \frac{I^2 N^2 \rho_{Cu}}{4h^3 f_c h_c} \tag{3.11}$$

If we solve the differential Eq. (3.9), ΔT can be expressed as a function of time as an increasing exponential that tends to ΔT_{max}.

$$\Delta T = -\frac{P_{el}}{h_c S} e^{-\frac{1}{\tau}t} + \frac{P_{el}}{h_c S} \qquad \text{where} \qquad \tau = \frac{\rho_v \, V c_{Cu}}{h_c S} \tag{3.12}$$

and ρ_v is the density of copper (8960 kg·m^3).

In order to prove the theoretical model (Eq. (3.12)) and simulate the behaviour described above, we have used finite element simulations made with the Siemens NX software. First, since we are taking into account the simplified model of the coil, we have done the simulations only considering a finite-length copper circumference of square cross-section and applying to this solid a power per unit volume of P_{el}/V, where V is the entire volume of the solid which is $V = 2\pi R h^2 = l a_{cond}/f_c$. Eq. (3.13) is the expression for the power dissipated per unit of volume:

$$\frac{P_{el}}{V} = \frac{P_{el}}{l a_{cond}/f_c} = \frac{I^2 \rho_{Cu} l/a_{cond}}{l a_{cond}/f_c} = \frac{I^2 \rho_{Cu} f_c}{a_{cond}^2} = \frac{I^2 \rho_{Cu} f_c}{(\pi (d/2)^2)^2} = \frac{16 I^2 \rho_{Cu} f_c}{\pi^2 d^4} \tag{3.13}$$

Then, we can put Eq. (3.10) in terms of $P_{el}\ /V$ and it can be written as:

$$\Delta T_{max} = \frac{P_{el}}{V} \frac{h}{4h_c} \tag{3.14}$$

For the first simulation, we have taken $R = 114.714$ mm, $h = h_{op} = 1.89737 \cdot 7.5 = 14.230$ mm, $I = 2.651$ A and $N = 72$ turns, which are the values obtained in the above section. In addition, as in the theoretical model, we have considered that all the generated power per unit of volume is dissipated to environment entirely through convection. It is also worth saying that we have assumed 20°C for the environment temperature and a convective heat transfer coefficient to air (h_c) of 10 W/m^{2}K [10]. If we make the analytical calculations with the indicated data, $P_{el}/V = 23\,814.02$ W/m^3 and ΔT_{max} results 8.47°C. With the simulation, the maximum temperature that the coil achieves is about 28.46°C. Thus, as we can see in Fig. 3.9, the simulation only considering the coil without any support fits almost perfectly the analytical solution obtained with the explained theoretical model.

Moreover, we have run two simulations more adding to the copper circumference the structure where the copper will be winded. Thus, we have taken into account natural convection in faces in contact with the environment and heat conduction between the coil faces in contact with the support assembly faces, which have a thickness of 5 mm. We have done simulations considering two different materials for the support: ABS (plastic) and aluminium.

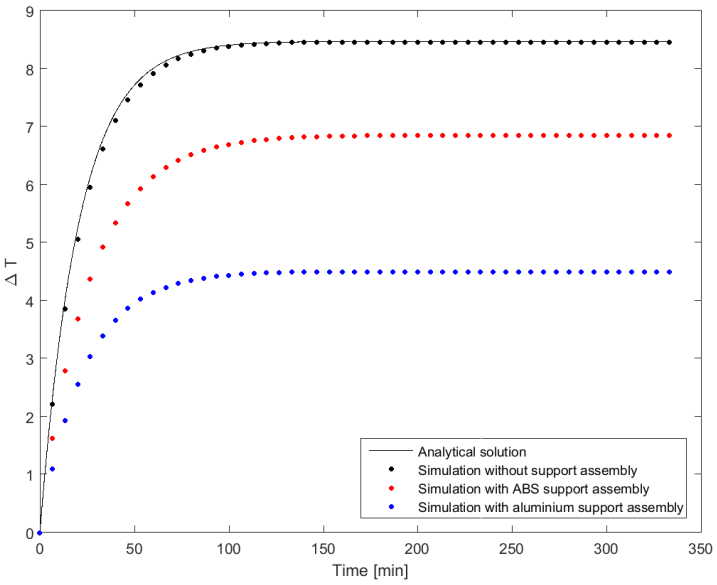

Figure 3.9: ΔT evolution as a function of time.

Fig. 3.9 shows that with an ABS support, the temperature reached (26.85°C) is lesser than without the support due to the increase of the surface throw which the heat can be dissipated. In Fig. 3.10 we can see how the coil and the support are heated at different times. As expected, the temperature of the copper part is always larger than the temperature of the ABS support.

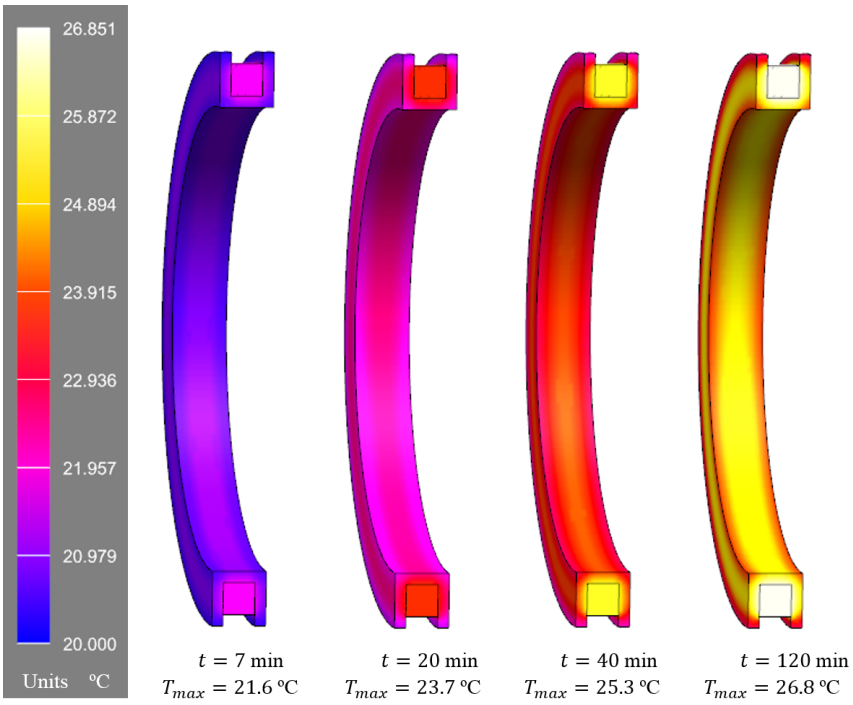

Figure 3.10: Thermal evolution using ABS support.

Furthermore, we have also done the simulation taking into account an aluminium support. We can use conductive material supports because our Helmholtz coils will work at constant current (CC) and thus, Eddy-currents cannot appear. In this case, as a result of the higher thermal conductivity of the aluminium, the temperature increase of the coil is only of 4ºC and besides, the copper part and the aluminium support heat up to the same temperature in a specific time.

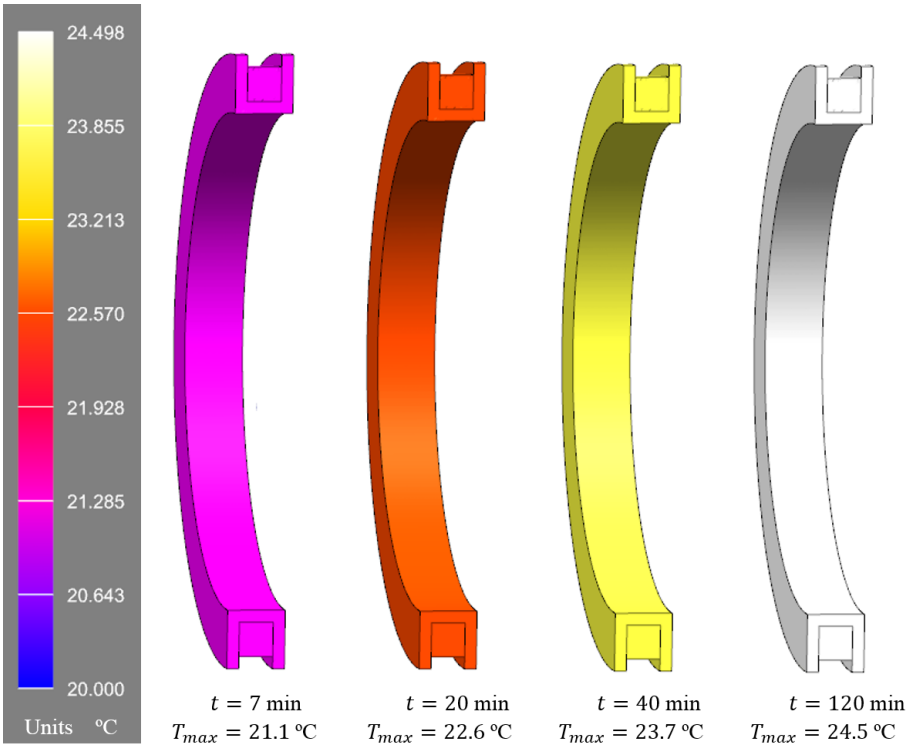

Figure 3.11: Thermal evolution using aluminium support.

After running this simulations, we realize that the time constant of the heating (τ) process is quite large. For the case that we have taken into account $\tau \sim 20\,\text{min}$. We know that we will have to apply current to our Helmholtz coils only when measuring with the Hall probe and it should be enough with 10 or 20 seconds per measure. If we alternate the coil to which we give more power, we will avoid warming up unnecessarily any of them. As a consequence, it will be possible to generate larger magnetic fields for short periods of time.

At this point, we have analytical expressions for the magnetic field, the tolerance and for the temperature increase. Then, we are able to look for a compromise solution between the field, the tolerance and the induced heating. In the following section we use multi-objective optimization in order to find a solution (or a set of solutions) that satisfy the requirements listed in Tab. 3.1.

3.6 Multi-objective Optimization

Multi-objective optimization involves optimizing a number of objectives simultaneously. Usually the optimal solution of an objective function is different from that of the other and this fact gives rise to a set of optimal solutions known as Pareto optimal solutions. Due to the multiplicity of solutions, these problems are solved suitably using evolutionary algorithms which use a population approach in its search procedure. In this section we present a brief description of the principles of multi-objective optimization problems and we also explain how we solve our own problem using an specific evolutionary multi-objective optimization (EMO) algorithm (NSGA-II) [11].

The purpose of multi-objective optimization is to find a vector of decision variables which satisfies some constraints and optimises a vector function whose elements represent the objective functions. Without loss of generality, since objective functions are to be either minimized or maximized, we can state that the multi-objective optimization problem takes the following general form [12]:

$$\begin{array}{rll} \text{Minimize/Maximize:} & f_m(\mathbf{x}) & m = 1, 2, ..., M \\ \text{Subject to:} & g_j(\mathbf{x}) \geq 0 & j = 1, 2, ..., J \\ & h_k(\mathbf{x}) = 0 & k = 1, 2, ..., K \\ & x_i^{(L)} \leq x_i \leq x_i^{(U)} & i = 1, 2, ..., n \end{array}$$

$\mathbf{x} \in \mathbf{R}^n$ is the vector of n decision variables, it is represented by $\mathbf{x} = [x_1, x_2, ..., x_n]^T$ and $x_i^{(L)}$ and $x_i^{(U)}$ are vectors of lower and upper bounds, respectively. The solutions satisfying the constrains and variable bounds constitute a *feasible decision variable space* $S \subset \mathbf{R}^n$. Constraints are imposed by the particular characteristics of the environment or resources available, and they are expressed in form of mathematical inequalities $g_j(\mathbf{x}) \geq 0$ $(j = 1, ...J)$ or equalities $h_k(\mathbf{x}) = 0$ $(k = 1, ...K)$. K must be less than n because, on the contrary, the problem is said to be overconstrained since there are no degrees of freedom left for optimizing. Moreover, in multi-objective optimization the objective functions constitute a multi-dimensional space called *objective space*, $Z \subset \mathbf{R}^M$. For each solution $\mathbf{x}$ in the decision variable space, there exists a point $\mathbf{z} \in \mathbf{R}^M$ in the objective space denoted by $\mathbf{f}(\mathbf{x}) = \mathbf{z} = [z_1, z_2, ..., z_M]^T$. (See Fig. 3.12)

For clarity and simplicity of the treatment we assume that all the objective functions are to be minimized. If an objective function f_m is to be maximized, it is equivalent to minimize the function $-f_m$. Having said that, we can handle the concept of optimality from the definition of dominance and the definition of Pareto optimality [13].

Definition 3.6.1 *If* $\mathbf{f}(\mathbf{x_1}) = [f_1(\mathbf{x_1}), ..., f_m(\mathbf{x_1})]$ *and* $\mathbf{f}(\mathbf{x_2}) = [f_1(\mathbf{x_2}), ..., f_m(\mathbf{x_2})]$ *denote two solution vectors,* $\mathbf{x_1}$ *is said to dominate* $\mathbf{x_2}$*, as notated by* $\mathbf{x_1} \succ \mathbf{x_2}$ *iff* $\forall m$*:* $f_m(\mathbf{x_1}) \leq f_m(\mathbf{x_2})$ *and* $\exists m$*:* $f_m(\mathbf{x_1}) < f_m(\mathbf{x_2})$*.*

All points which are non dominated by another member of the set are called non-dominated points. These points make up a front when viewed them together on the objective space (*non-domination front*) [14].

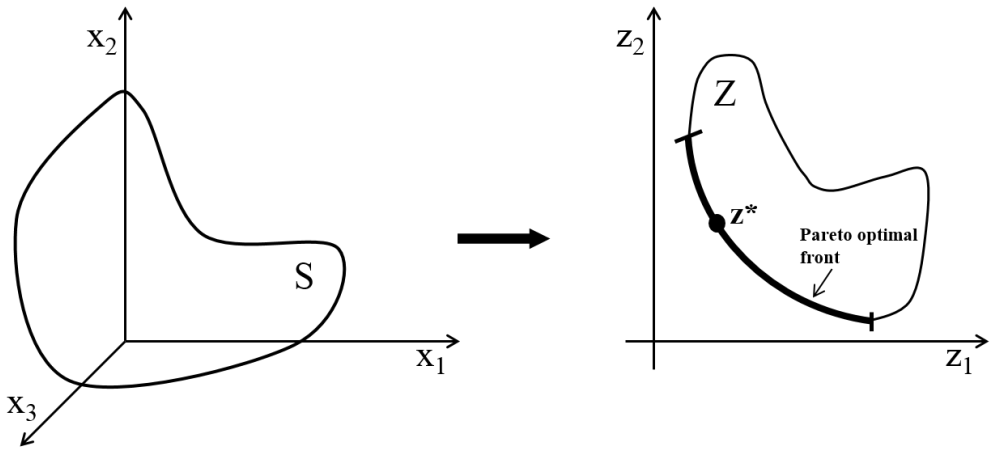

Figure 3.12: Diagram illustrating the *feasible decision variable space* (S) and the *objective space* (Z). The thick line contains all the Pareto optimal objective vectors (Pareto optimal front). The vector z^* is an example of them.

Definition 3.6.2 *A decision vector* $\mathbf{x}^* \in S$ *is Pareto optimal if there does not exist another decision vector* $\mathbf{x} \in S$ *such that* $f_m(\mathbf{x}) \leq f_m(\mathbf{x}^*)$ *for all* $m = 1, ..., M$ *and* $f_l(\mathbf{x}) < f_l(\mathbf{x}^*)$ *for at least one index* l.
An objective vector $\mathbf{z}^* \in Z$ *is Pareto optimal if there does not exist another objective vector* $\mathbf{z} \in Z$ *such that* $z_m \leq z_m^*$ *for all* $m = 1, ..., M$ *and* $z_l < z_l^*$ *for at least one index* l*; or equivalently,* $\mathbf{z}^*$ *is Pareto optimal if the decision vector corresponding to it is also Pareto optimal.*

To sum up, a solution is called nondominated or Pareto optimal if non of the objective functions can be improved in value without degrading some of the other objective values. Points lying on the non-domination front, by definition, do not get dominated by any other point in the objective space, hence are Pareto-optimal points (together they constitute the Pareto-optimal front) and the corresponding decision variable vectors are called Pareto-optimal solutions.

Mathematically, every Pareto optimal point is an equally acceptable solution of the multi-objective optimization problem and, since it is generally desirable to obtain one point as solution, is the person solving the problem who selects this point depending on other information that it is not contained in the objective functions.

3.6.1 Optimization of Helmholtz coils parameters using NSGA-II EMO algorithm

NSGA-II is an evolutionary multi-objective optimization algorithm developed by K.Deb. which attempts to find multiple Pareto-optimal solutions in a multi-objective optimization problem. We have used NGPM (NSGA-II Program in Matlab) [15], which is the implementation of NSGA-II in Matlab in order to know the parameters characterizing a Helmholtz pair that satisfies our wish-list.

We take as decision variables N, I, R and h. In our case, the objectives functions are B, the tolerance and ΔT, which have the following expressions:

$$\begin{cases} B = \left(\dfrac{4}{5}\right)^{3/2} \mu_0 \dfrac{NI}{R} \\ \text{Tol} = \dfrac{12000(5h^2s^2 + 324s^4)}{124h^4 - 125h^2R^2 + 7500R^4 + 30240s^4} \\ \Delta T = \dfrac{I^2N^2\rho_{Cu}}{4h^3 f_c h_c} \end{cases} \tag{3.15}$$

We run NSGA-II with a population size of 400 and for 100 generations. Moreover the bounds specified for each decision variable are $N \in [60, 400]$, $I \in [0.1, 2.65]$ A, $R \in [0.1, 0.13]$ m and $h \in [0.014, 0.03]$ m, and the objective functions must satisfy $B \geq 50$ G, Tol$\leq 0.01\%$ and $\Delta T \leq 20$°C. These three restrictions correspond to the constraints of our problem.

Once the simulation has finished, in Fig. 3.13 we see that all the solutions are situated in the objective space forming a surface, since there are three objective functions. As mentioned, all the solutions situated in this surface are acceptable solution of our multi-objective optimization problem. So, we can choose any point from this set as our final solution.

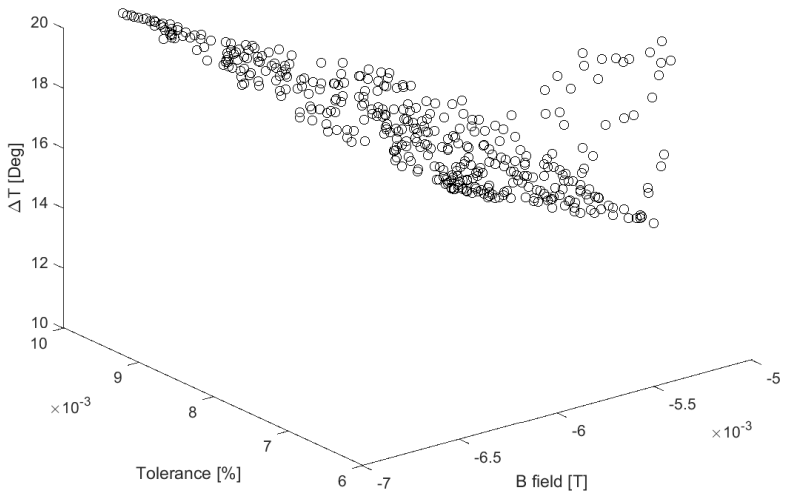

Figure 3.13: Pareto-optimal front. All points of this set are valid solutions for our problem.

Then, we decide to make the projection of the set of points on the Tol-ΔT plane and take the data of the red point in Fig. 3.14. We have chosen this point because we can see that any other point that would decrease considerably the temperature, will increase the tolerance and other points that would allow us to decrease more the tolerance will increase greatly the temperature. Moreover, we think that the values obtained of N, R and h are reasonable to manufacture the coil.

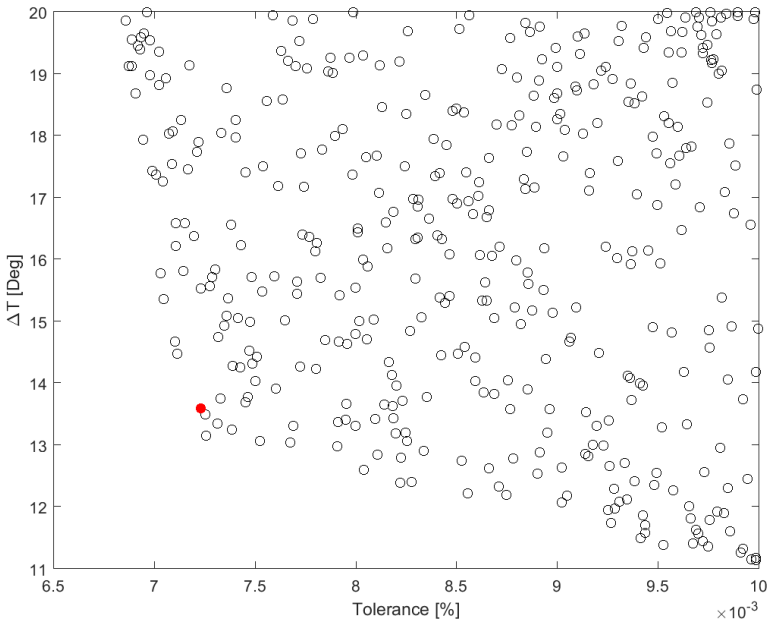

Figure 3.14: Plane Tol-ΔT where the red point is the chosen solution.

N	I [A]	R [mm]	h [mm]	B [G]	Tol [%]	ΔT [°C]
323	2.28	129.7	30	50.98	0.00723	13.59

Table 3.6: Values that correspond to the red point.

The result obtained is indicated in Tab. 3.6. With this values, we can calulate d, which results 1.5 mm. From this data and taking into account coil winding, we can adjust the coil parameters that will correspond to one Helmholtz pair and then, we will be able to find the parameters of the other two pairs of coils. All the calculations are explained in the following section.

3.7 Coil manufacturing

Coil winding is the manufacture of electromagnetic coils. For the design of our coils, we have taken into account round wires arranged forming an orthocyclic winding (See Fig. 3.15). It is a multi-layer winding in which the round wires in the upper layer are in the grooves of the lower layer and they all occupy a dense package.

For the coil manufacturing we have decided to use grade 2 enamelled copper wire with a conductor/total diameter of 1.5/1.571 mm. This wire has been selected because it is thin enough so as to enable the usage of standard coil winding equipment, and at the same time it provides a higher conductor/insulation ratio in comparison to thinner wires, thus delivering a higher filling factor f_c.

Since we need an integer number of turns, we have to adjust N obtained in Tab. 3.6 so that it can be written as a product of n and m ($N = m \cdot n$), where n is the number of layers and m is the number of wires in each layer. Given the compaction of the layers in the vertical direction, in order to end up having more or less a square coil section, n must be larger than m. In the range of turns where we are moving, where both m and n will have values between 15 and 30, the excess of n above m should be between 3 and 4.

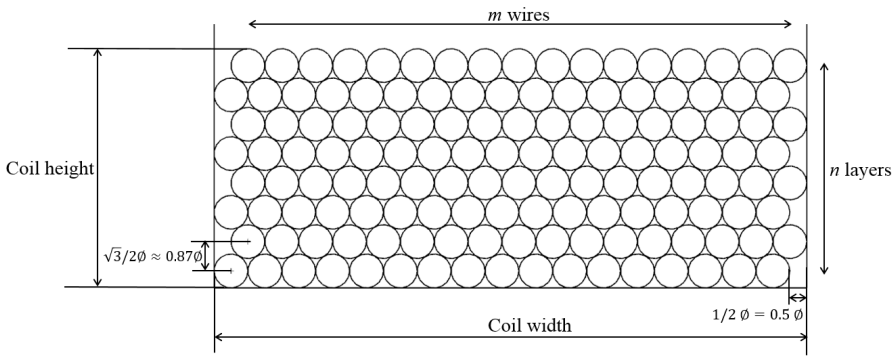

Figure 3.15: Orthocyclic winding

Once N has been determined, Eq. (3.16) is used to calculate the width and the height of the coil and then, multiplying both values, the area of the coil cross section can be inferred.

$$\begin{aligned} \text{Coil width} &= (m + 0.5)\varnothing \\ \text{Coil height} &= [1 + 0.87(n + 1)]\varnothing \end{aligned} \tag{3.16}$$

where $\varnothing$ is the effective diameter. We have taken $\varnothing = 1.6$ mm to do the calculation, which is slightly larger than the nominal diameter of the wire, so we will have some margin to accommodate irregularities in the wire and winding errors.

It is worth saying that we want to maintain the value of I indicated in Tab. 3.6 (~ 2.3 A) and readjust R. Then, we have to recalculate R with Eq. (2.7) in order to obtain a magnetic field of 50 G and we can also recalculate the value of the filling factor using $f_c = N\pi(\varnothing^2/4)/A$. Thus, the filling factor results 0.77.

Finally, we can also calculate the electrical power dissipated by a coil and its resistance using Eq. (3.9) and Eq. (3.3) respectively and ΔT_{max}, which has a new expression since we have a rectangular coil section.

$$\Delta T_{max} = \frac{2I^2 \rho_{Cu} N}{\pi d^2 h_c (w + h)} \tag{3.17}$$

where w is the coil width and h is the coil heigh.

Once we have well characterized one pair of coils, we need to add two pairs of orthogonal coils more in order to generate a known magnetic field in an arbitrary direction. These two pairs of coils must be enlarged with respect to the first pair to avoid any mechanical interference. In our case, we have chosen a scale factor from pair to pair of 1.35, with the aim of leaving enough space between coils to accommodate the elements of the support system. Apart from increasing the radius of the coils, the number of turns and the coil cross section have also to be readjusted using the same scale factor to provide the same magnetic field intensity at nominal current in the three pairs of coils. Then, we will obtain again a decimal N and we will have to follow the previous process to achieve the definitive results. The data used to make the calculus and the results obtained are listed in Tab. 3.7.

In Tab. 3.7 we can appreciate the effects of enlarging the coils: the value of N increases, there is an improvement in the value of the tolerance and the heating of the system gets worse, but it is nevertheless maintained below the 20°C that we require.

3.8 Setup specifications

Current [A]	2.3
j [A/mm²]	1.3
Conductor diameter [mm]	1.5
Effective diameter ⌀[mm]	1.6
Filling factor (f_c)	0.77

Copper Resistivity [Ω·m]	1.7E-08
Air convect.coef. [W/(m²·K)]	10

	Coils X (small)	Coils Y (medium)	Coils Z (large)
Radius [mm]	125.74	172.89	236.59
Maximum Radius [mm]	139.07	188.31	254.79
Minimum Radius [mm]	112.41	157.48	218.39
Coil Cross Section [mm²]	703.72	961.96	1310.40
Coil width (w) [mm]	26.40	31.20	36.00
Coil height (h) [mm]	26.66	30.83	36.40
m wires	16	19	22
n layers	19	22	26
Number of turns	304	418	572
B field [G]	49.96	49.97	49.98
Tolerance [%]	7.83E-03	2.44E-03	6.97E-04
ΔT [ºC]	14.58	17.15	20.10
Power/coil [W]	12.22	23.11	43.27
Resistance/coil [Ω]	2.31	4.37	8.18

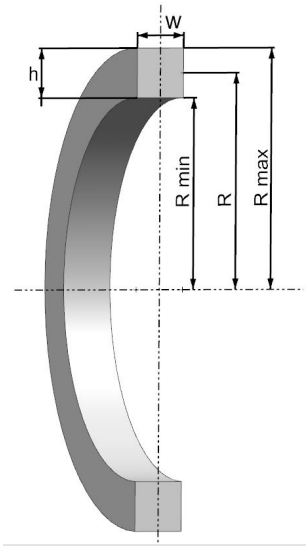

Table 3.7: Design parameters for the 3 sets of coils for the 3D Helmholtz system and the resulting B, tolerance, ΔT, power/coil and resistance/coil obtained by means of the simulations. A scheme of the parameters of a coil is also shown.

General view

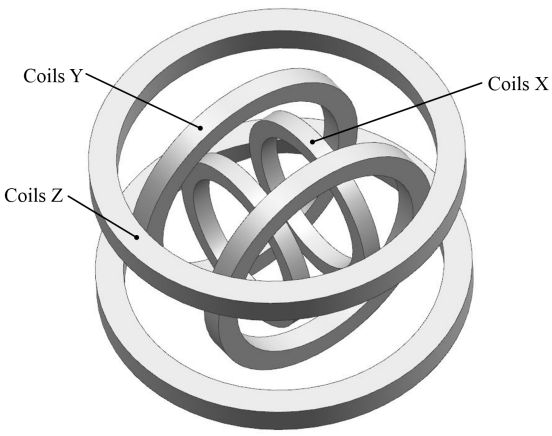

Figure 3.16: General view of the system of 3D Helmholtz coils.

3.9 Mechanical tolerances

Once we have determined the design parameters for the three sets of coils of the 3D Helmholtz system (Tab. 3.7), we want to know how the tolerance varies within the volume 15x15x15 mm^3 and how the magnetic field changes in the midpoint of a non ideal pair of Helmholtz coils taking into account different possible sources of error. In this section, we analyse the effect of a rotation α of one coil with respect to the other and the effect of a displacement τ between their centres. Apart from these two sources of misalignment, we also study the case of having a separation between the midplanes of the coils of $(R + \eta)$ mm and the situation of having one coil with a radius δ mm larger than that of the other coil.

In the first case, we have two coils with the centre on the same axis (x axis) but they are not parallel. In order to simulate with RADIA the effect of the non-perpendicularity of one coil with its axis, we vary the angle with respect to the vertical (α) of one of the coils, in an interval from 0° to 5° (0.087 rad) each 0.2^o (0.0034 rad). By the contrary, in the second case, the two coils are parallel, but the axes of both coils are not perfectly aligned, there is displacement between their centres. We vary the vertical distance between the two centres (τ) in a range from 0 mm to 10 mm each 0.5 mm, to see the effect that this displacement has on the tolerance and on the magnetic field.

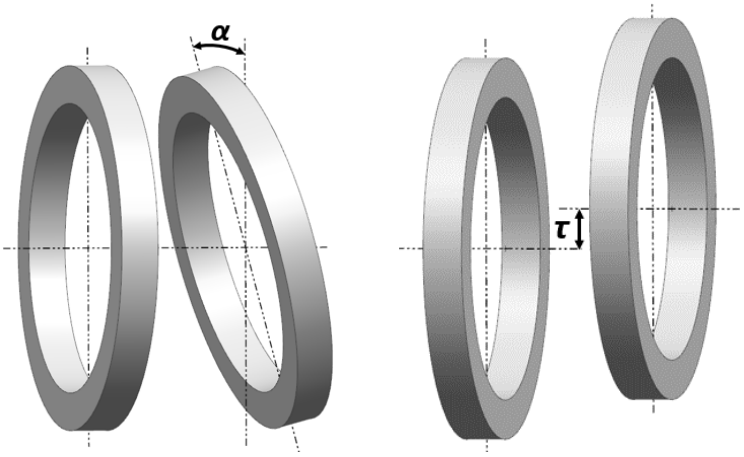

Figure 3.17: Sources of misalignment of each pair of coils.

Fig. 3.18 shows that the tolerance increases as the values of α and τ are increased. For the case of the smallest pair of coils (Coils X) we have the following behaviour:

$$\begin{aligned} \mathrm{Tol}(\alpha) &= 0.00782540 + 11.2000\ \alpha \\ \mathrm{Tol}(\tau) &= 0.00782540 + 0.00898328\ \tau + 0.000861055\ \tau^2 \end{aligned} \tag{3.18}$$

When α and τ are perfectly zero, Tol = 0.0078254%, which is the value specified in Tab. 3.7. If we want that the maximum tolerance to be 0.01% in order to fulfil the specifications indicated in Tab. 3.1, the maximum value of α that we can allow is 0.2 mrad (0.01^o) and the maximum value of τ is 0.237 mm.

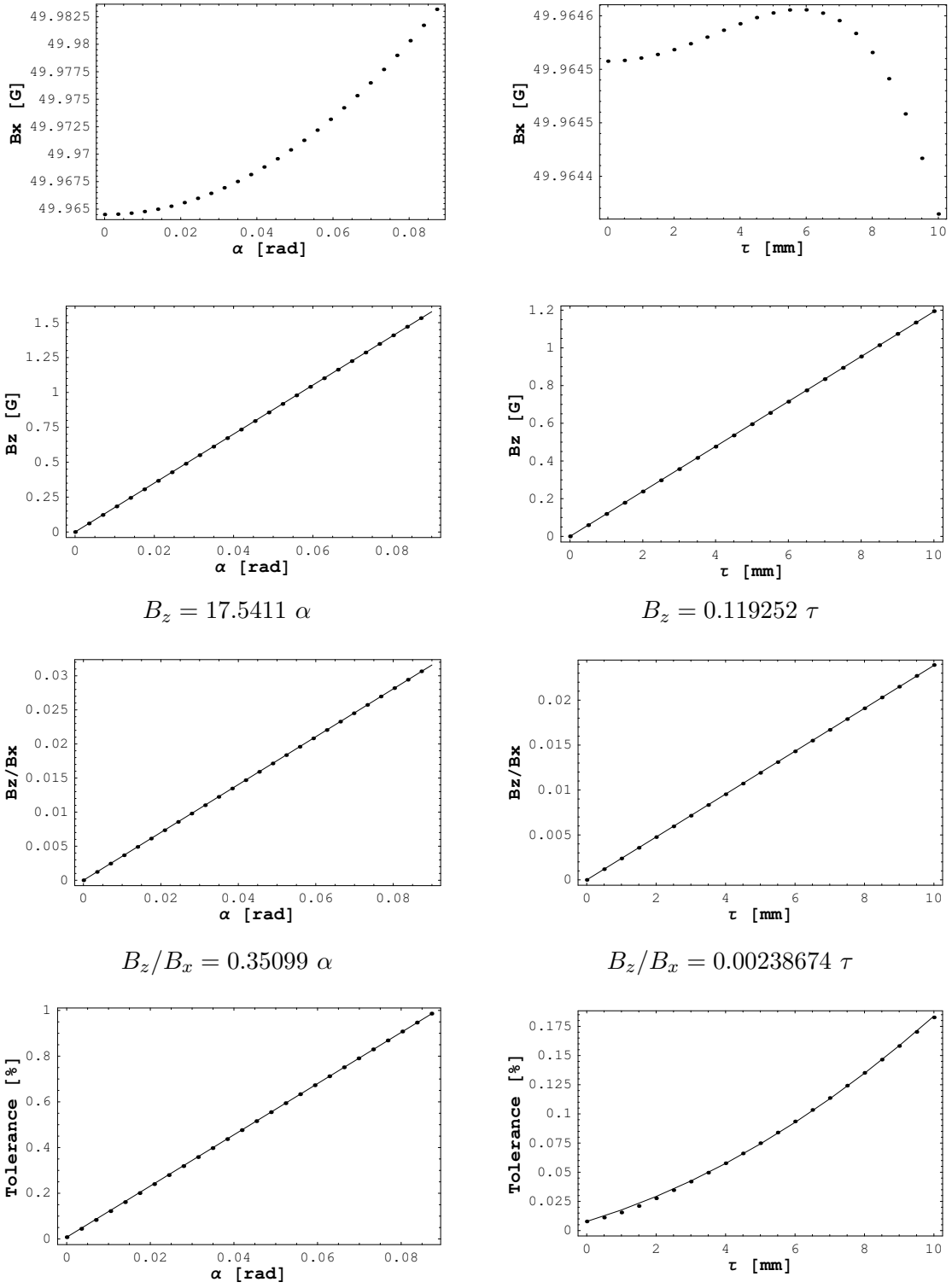

$B_z = 17.5411\ \alpha$

$B_z = 0.119252\ \tau$

$B_z/B_x = 0.35099\ \alpha$

$B_z/B_x = 0.00238674\ \tau$

$\mathrm{Tol} = 0.00782540 + 11.2000\ \alpha$

$\mathrm{Tol} = 0.00782540 + 0.00898328\ \tau + 0.000861055\ \tau^2$

Figure 3.18: B_x, B_z, B_z/B_x and the tolerance as a functions of α and τ. This results have been obtained considering the design parameters and the orientation of the smallest coils (Coils X).

Furthermore, when the two coils of each pair are not perfectly aligned, the generated magnetic field has an angular deviation with respect to the nominal axis of the pair. Thus, if we consider the pair of coils whose vertical axis is z and with the nominal axis parallel to x (Coils X), if α and τ increase (See Fig. 3.17), although B_x remains the main component of the magnetic field, the component B_z increases linearly (minority component).

The minority component will limit the accuracy of our system, since we want to guarantee the orthogonality of the magnetic fields generated by the three pairs of coils. To do that, we must keep the deviation of the magnetic field produced by each pair of coils below the alignment requirement of the whole system indicated in Tab. 3.1 (0.2 mrad). So, our objective is to achieve $B_{minority}/B_{main} \leq 0.2\,\text{mrad}$ for each pair of coils. In the case that we are considering, we have obtained the following expressions:

$$\begin{aligned} B_z/B_x &= 0.35099\ \alpha \\ B_z/B_x &= 0.00238674\ \tau \end{aligned} \tag{3.19}$$

Then, the inequality that we have to fulfil is $B_z/B_x \leq 0.2\,\text{mrad}$. This also sets a tolerance for the maximum permitted values of α and τ. Applying $B_z/B_x = 0.2\,\text{mrad}$ to Eq. (3.19) we obtain $\alpha = 0.57\,\text{mrad}$ and $\tau = 0.084\,\text{mm}$.

	Parameter	Coils X	Coils Y	Coils Z
Tol	**Angular deviation α [mrad]**	0.19	0.94	1.59
	Centres offset τ [mm]	0.23	1.81	3.91
B_z/B_x	**Angular deviation α [mrad]**	0.57	0.57	0.57
	Centres offset τ [mm]	0.084	0.12	0.16

Table 3.8: Mechanical tolerance for the alignment of each pair of coils.

In Tab. 3.8 are listed the mechanical tolerances for the alignment of each pair of coils calculated using the expression for the tolerance and also using the equation for B_z/B_x. We can see that, as the radius of the coils increase, the values permitted for α and τ are larger. This is because the tolerance, when $\alpha = \tau = 0$, is getting smaller. Nevertheless, we would like to achieve for the three pairs of coils the most restrictive values of the table (in green), which correspond to the ones of the smallest coils.

Another source of error that can appear during the process of construction is not having the two coils of a pair separated by a distance equal to their radius (non ideal Helmholtz coil). Thus, the distance between both coils is equal to $R + \eta$. We have evaluated this possible imperfection using the data of Coils X. As expected, the tolerance increase as η increase (See Fig. 3.19), B_x is the main component of the magnetic field and the components B_y and B_z remain practically zero. We have calculated that, if we want to maintain a tolerance of 0.01%, we can have as a

maximum value $\eta = 0.25\,\text{mm}$. This is an easily achievable tolerance and it will not cause any problem during the assembly process.

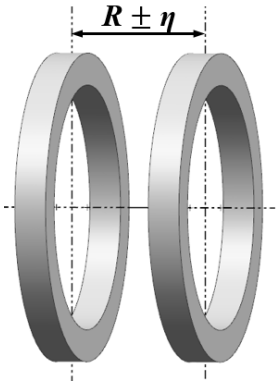

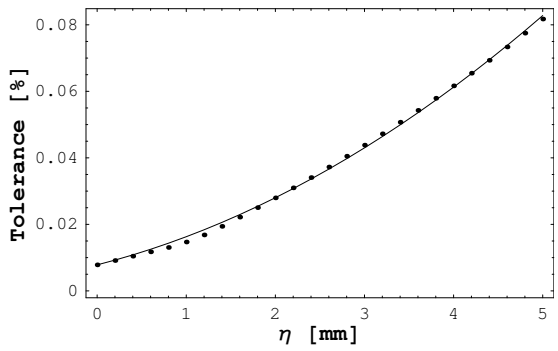

$$\text{Tol} = 0.00782540 + 0.00683059\ \eta + 0.00163211\ \eta^2$$

Figure 3.19: Tolerance as a function of η.

Finally, the fourth source of error that we study is the fact of having one coil with a radius $\delta\,\text{mm}$ different than that of the other coil. This can happen due to imperfections during the process of coil winding. To run this simulation we consider one coil with a radius R and another coil with a radius $R + \delta$ and we evaluate the tolerance as a function of δ. Fig. 3.20 shows the results obtained for Coils X and the value of δ must be $0.019\,\text{mm}$ to have a tolerance of 0.01%. This result indicates us that is important to achieve a very accurate and precise winding.

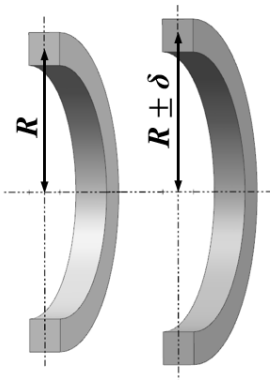

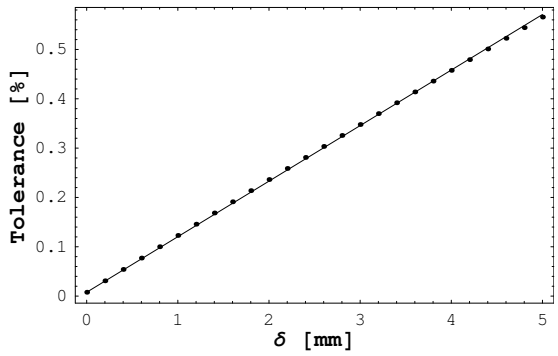

$$\text{Tol} = 0.00782540 + 0.112616\ \delta$$

Figure 3.20: Tolerance as a function of δ.

To sum up, after calculating the permitted values for all the possible sources of error considered, we see that the tolerances permitted are very restrictive and thus, it is important a precise machining of the pieces where the conductor is allocated and an accurate winding.

4 | 3D Helmholtz coils construction

4.1 Mechanical design

We have designed three pairs of cylindrical aluminium supports (one for each of the coils) which have a rectangular groove with the appropriate dimensions where the wired wire will be allocated. For the back of each of these pieces, we have provisionally attached a rectangular piece with a hole in the centre that is coaxial with the axis of the coil, in order to be able to position the assembly correctly on the winding machines. In Fig. 4.1, we can see some holes along the perimeter of the aluminium cylinder that will be used to introduce the epoxy resin to make the winding be well compact and at the same time, they will reduce the weight of the set, since only the weight of the copper has been estimated to be of a total of 50 kg.

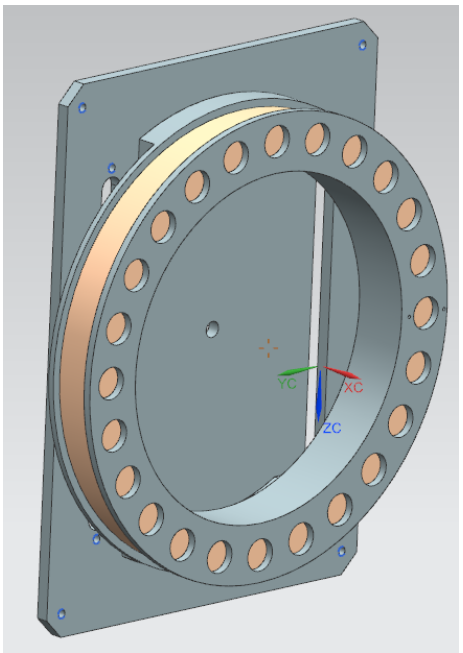

Figure 4.1: Representation of the coil with its support attached to the rectangular piece used to adapt the support of our coils to the winding machine.

It should be noted that all supports have been designed so that they can be interlocked when assembling the whole set and they can allow the orthogonal arrangement between the different pairs of coils. All the pieces will be mechanized very precisely, which will guarantee that upon assembly the relative positioning of the coils will be close to the design values. In addition, these supports will provide a cylindrical surface concentric with the axis of each coil and a flat surface parallel to the plane of the coil. Therefore, once assembled it will be possible to measure any misalignment between the coils by means of a laser tracker or a portable coordinate measuring machine and, if necessary, to correct it by means of the introduction of shims. Fig. 4.2 shows a view of the assembled system. In the Appendix we present the set of drawings done to construct our system of 3D Helmholtz coils.

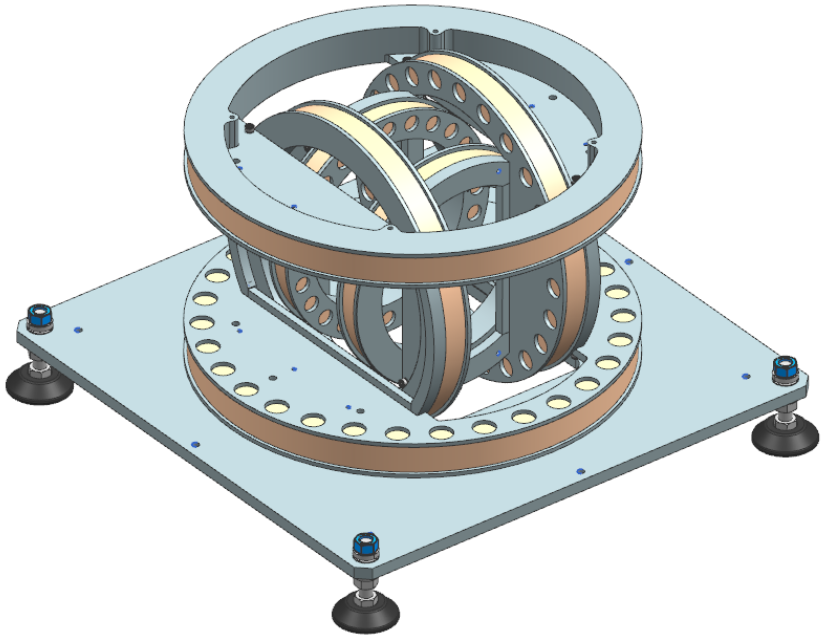

Figure 4.2: Drawing of the assembled system.

The coils of each pair will be connected in series and thus, three power supplies of constant current will be used. Besides this, we have estimated that the maximum operating current ($\lesssim 5\,\mathrm{A}$) and power ($< 100\,\mathrm{W}$) required for the wire will sit comfortably inside the range provided by the power supplies available at our laboratory.

4.2 First prototype

Before constructing the entire system, we have decided to manufacture first a prototype of only one coil, in order to validate the winding process since it must be very precise. Given the dimensions of the coils, the tolerances that have been established and the mechanical demands, we have decided that the mechanical parts (supports of the coils) will be manufactured in the ALBA Synchrotron workshop and the coil winding will be outsource to a specialized local company.

By the moment, the support for the smallest coil has been manufactured (See Fig. 4.3) and soon it will be send to the specialized company to make the winding.

Figure 4.3: Support for the prototype of one coil.

5 | Conclusions and further work

In this bachelor's thesis we have presented the design of the system of 3D Helmholtz coils with the objective of calibrating the Hall probes used at ALBA magnetic measurements laboratory with more accuracy.

The first days of my stay at ALBA Synchrotron I understood why there was a need of finding a new calibration system for the Hall probes, which would allow us to improve the determination of the three magnetic field components generated by the magnets that are characterized at the laboratory, as well as the decision to build the calibration equipment that is designed in this thesis. At the same time, so as to carry out all the design process, I had to get used to working with the magnetostatic simulation code RADIA and to perform thermal simulations with the Siemens NX software.

In order to achieve the design that fulfils our requirements, different simulations have been performed, whose results have coincided with the values obtained with the analytical expressions deduced in this thesis. From these calculations, we have inferred how the different variables involved in our problem behave (coil radius, conductor diameter, number of turns and current applied). Then, with the help of the NGPM (NSGA-II Program in Matlab) and having into account orthocyclic winding, we have been able to find a compromise solution to optimize the associated merit figures (magnitude and homogeneity of the generated magnetic field and the heating of the system). We have also defined a very restrictive construction tolerances to achieve the desired magnetic field quality.

Once the design parameters of our system have been defined, the set of drawings for its manufacture has been prepared. Given the dimensions of the coils, the tolerances that have been established and the mechanical demands, we have decided that the mechanical parts (supports of the coils) will be manufactured in the ALBA Synchrotron workshop and the coil winding will be outsource to a specialized local company. In order to validate the winding process and make all the relevant checks before ordering the definitive construction of the entire system, it has been decided to build a first prototype of a single coil. Hence, we expect to have the system ready by Summer 2019 and we intend to experimentally validate its operation by calibrating the Hall effect probes during the second half of the year.

In conclusion, we have managed to design a system that allows generating a magnetic field of 50 G, of homogeneity 10^{-4} within a volume of 15x15x15 mm^3 without overheating due to the dissipated power during its operation. In addition, we have verified that the time constant of the heating process is longer than 20 min and therefore, it will be possible to generate larger magnetic fields for short periods of time. With this system of Helmholtz coils, it is expected to achieve an accuracy in the calibration of the Hall effect probes of 0.2 mrad, which would substantially improve the current 10 mrad.

Special attention should be given to reference [16], an article that has emerged from this work. This article was presented at IPAC conference in Melbourne on May 2019.

References

[1] Merriam-Webster, https://www.merriam-webster.com/dictionary/Helmholtz%20coil

[2] S. Sanfilippo, "Hall probes: physics and application to magnetometry", in *Proc. of CAS-CERN Accelerator School: Magnets* (June 2009), 2010, ISBN 978-92-9083-355-0, p. 423

[3] J. Marcos, V. Massana, L. García and J. Campmany, "Latest developments at the ALBA magnetic measurement laboratory", *Meas. Sci. Technol.*, **29**, 024002, 2018. doi:10.1088/1361-6501/aa8ba2

[4] J. Campmany, J. Marcos, V. Massana, Z. Martí, "Construction & Commissioning of a 3D Hall probe bench for Insertion Devices measurements at ALBA Synchrotron Light Source", *IMMW15*, August 2007

[5] F. Bergsma, "Calibration of Hall sensors in three dimensions", *IMMW13*, May 2003, https://cds.cern.ch/record/1072471/files/cer-002727968.pdf

[6] O. Dunkel, D. Giloteaux, V. Remondino, S. Russenschuck, "A multi-purpose 3D-Helmholtz-Coil for high accuracy measurements and calibration", *IMMW20*, June 2017, https://aapt.scitation.org/doi/abs/10.1119/1.16309

[7] Th. Zickler, "Basic design and engineering of normal-conduction, iron-dominated electromagnets", in *Proc. of CAS-CERN Accelerator School: Magnets* (June 2009), 2010, ISBN 978-92-9083-355-0, p. 65

[8] P. Elleaume, O. Chubar and J. Chavanne, "Computing 3D Magnetic Fields from Insertion Devices", in *Proc. of PAC Conference PAC97*, Vancouver, Canada, May 1997, p. 3511. http://accelconf.web.cern.ch/accelconf/pac97/papers/pdf/9P027.PDF

[9] M.S. Crosser, S. Scott, A. Clark and P.M. Wilt "On the magnetic field near the center of Helmholtz coils", *Rev. Sci. Instrum.*, **81**, 084701, 2010. doi:10.1063/1.3474227

[10] A.J. Chapman, *Fundamentals of heat transfer*, Macmillan Publishing Company, USA, 1987

[11] K. Deb, A. Pratap, S. Agarwal and T. Meyarivan, "A Fast and Elitist Multiobjective Genetic Algorithm: NSGA-II", *IEEE Transactions on Ecolutionary Computation*, Vol. 6, No. 2, p. 182-197, April 2002, doi:10.1109/4235.996017

[12] K. Deb, "Multi-Objective Optimization Using Evolutionary Algorithms: An Introduction", *KanGAL Report*, No.2011003, Indian Institute of Technology Kanpur, February 2011, https://www.egr.msu.edu/ kdeb/papers/k2011003.pdf

[13] Kaisa M. Miettinen, *Nonlinear Multiobjective Optimization*, Kluwer Academic Publishers, USA, 1999

[14] C-W. Seah, Y-S. Ong, I.W. Tsang, S. Jiang, "Pareto Rank Learning in Multiobjective Evolutionary Algorithms", *IEEE World Congress on Computational Intelligence*, 2012, doi:10.1109/CEC.2012.6252865

[15] Song Lin, "NGPM–A NSGA-II Program in Matlab v1.4", *MathWorks*, July 2011, https://www.mathworks.com/matlabcentral/fileexchange/31166-ngpm-a-nsga-ii-program-in-matlab-v1-4

[16] A. Fontanet, J. Marcos, Ll. Ribó, V. Massana, J. Campmany, "Design and construction of 3D Helmholtz coil system to calibrate 3D Hall probes", *IPAC 2019*, Melbourne, Australia, May 2019, https://ipac2019.vrws.de/papers/thpts055.pdf

Appendix

Drawings

In this appendix we present the different drawings used to construct our system of 3D Helmholtz coils.

1. Support of Coils X.
2. Support of Coils Y.
3. Support of Coils Z.
4. Rectangular piece used to adapt the support of our coils to the winding machine.
5. Entire assembling of the system.

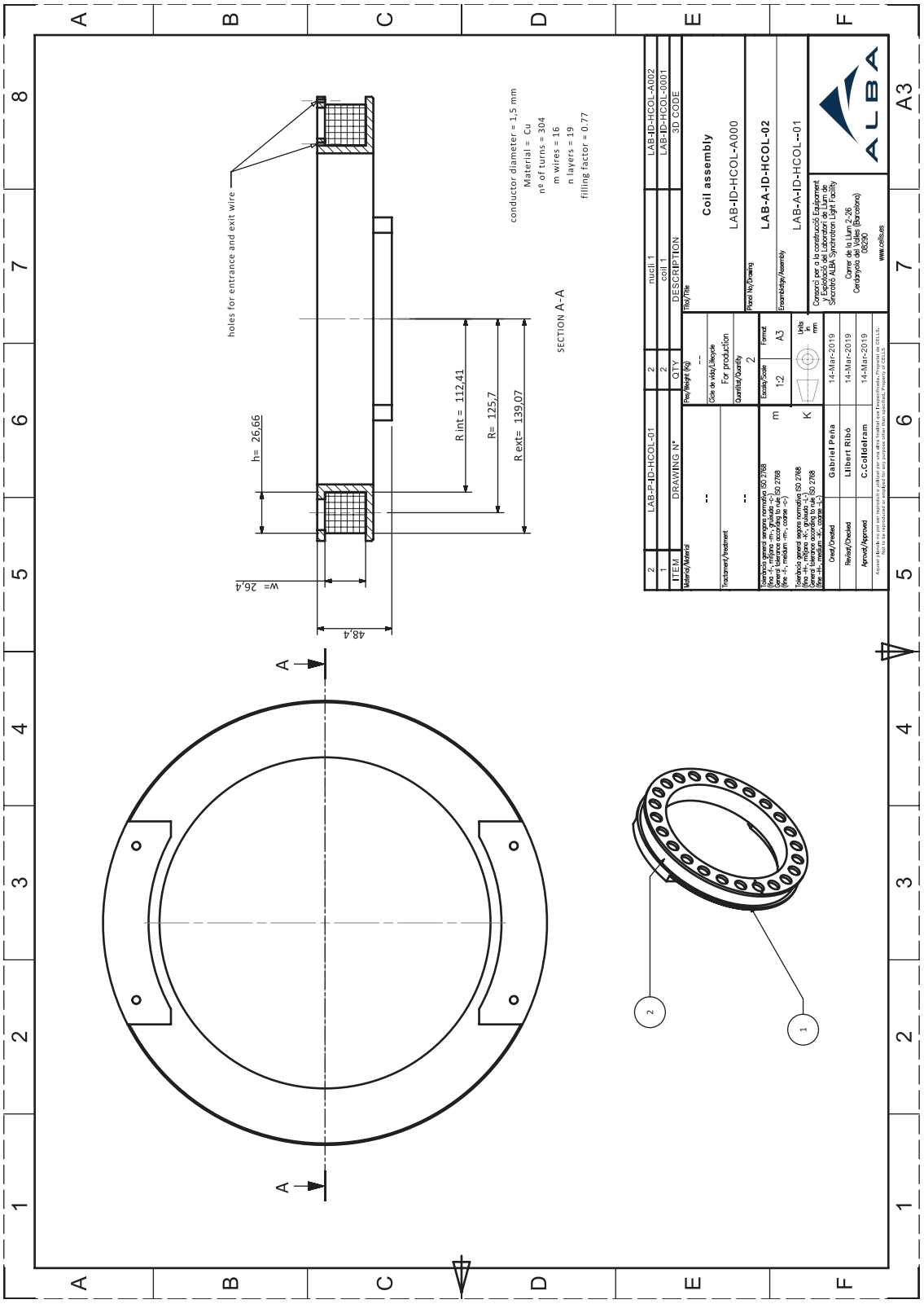
holes for entrance and exit wire
conductor diameter = 1,5 mm
Material = Cu
nº of turns = 304
m wires = 16
n layers = 19
filling factor = 0.77
SECTION A-A
h= 26,66
R int = 112,41
R= 125,7
R ext= 139,07
w= 26,4
48,4
A
A
2
1
LAB-P-ID-HCOL-01
DRAWING Nº
--
Tractament/Treatment
--
Material/Material
--
Peso/Weight (Kg)
--
Cicle de vida/Lifecycle
For production
Quantitat/Quantity
2
Escala/Scale
1:2
Format
A3
Unitats
mm
nucli 1
coil 1
DESCRIPTION
Títol/Title
Coil assembly
LAB-ID-HCOL-A000
Plano No/Drawing
LAB-A-ID-HCOL-02
Ensamblatge/Assembly
LAB-A-ID-HCOL--01
LAB-ID-HCOL-A002
LAB-ID-HCOL-0001
3D CODE
Consorci per a la construcció Equipament
y Explotació del Laboratori de Llum de
Sincrotró ALBA-Synchrotron Light Facility
Carrer de la Llum 2-26
Cerdanyola del Vallès (Barcelona)
08290
www.cellsa.es
ALBA
A3
Dibuixat/Drawed
Gabriel Peña
14-Mar-2019
Revisat/Checked
Llibert Ribó
14-Mar-2019
Aprovat/Approved
C.Colldelram
14-Mar-2019

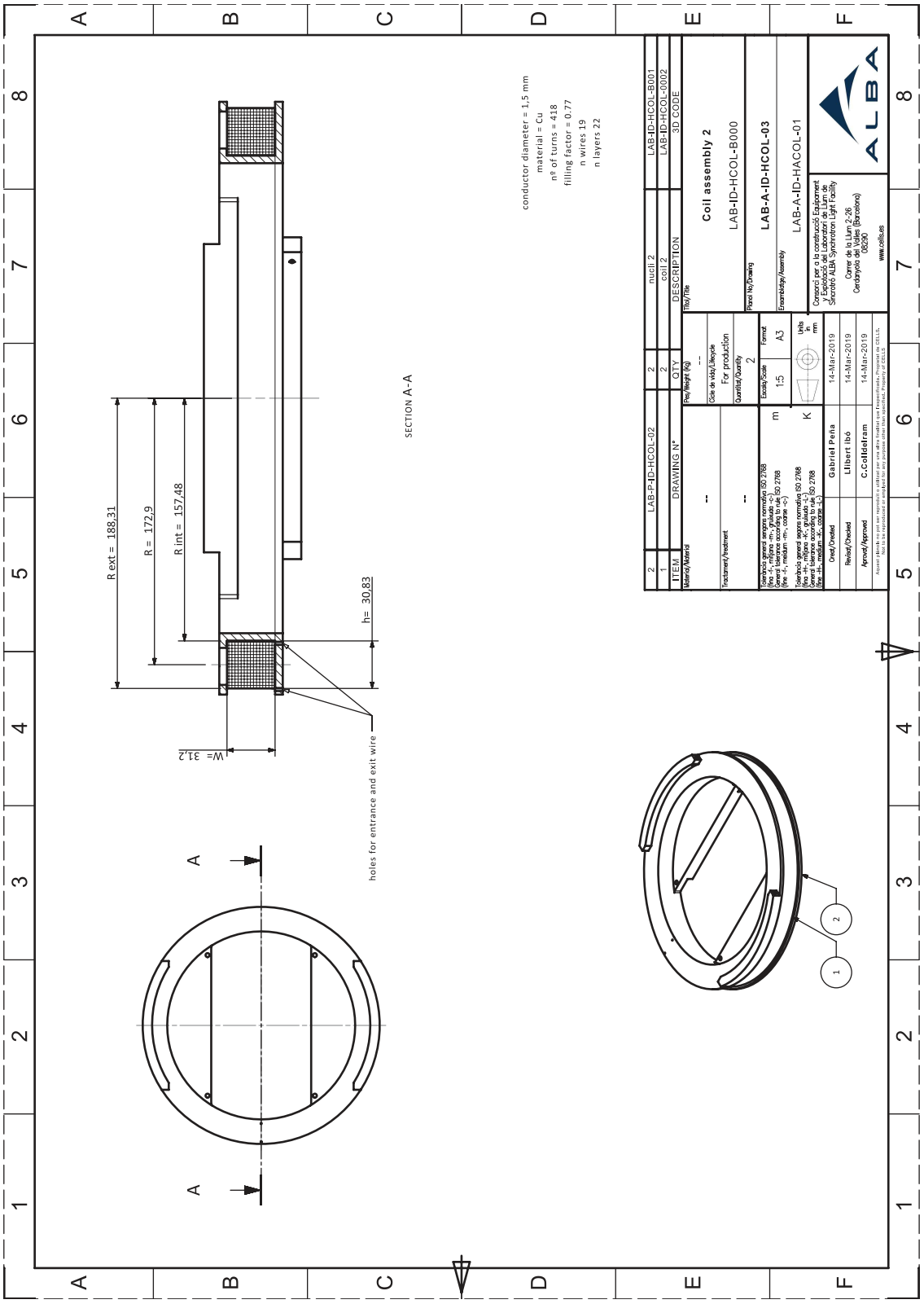
R ext = 188,31
R = 172,9
R int = 157,48
h= 30,83
W= 31,2
holes for entrance and exit wire
SECTION A-A
conductor diameter = 1,5 mm
material = Cu
nº of turns = 418
filling factor = 0,77
n wires 19
n layers 22
LAB-P-ID-HCOL-02
DRAWING Nº
Coil assembly 2
LAB-ID-HCOL-B000
LAB-A-ID-HCOL-03
LAB-A-ID-HACOL-01
LAB-ID-HCOL-B001
LAB-ID-HCOL-0002
3D CODE
For production
Consorci per a la construcció, Equipament i Explotació del Laboratori de Llum de Sincrotró ALBA-Synchrotron Light Facility
Carrer de la Llum, 2-26
Cerdanyola del Vallès (Barcelona)
08290
www.cellis.es
Gabriel Peña
Llibert Ibó
C.Colldelram
14-Mar-2019

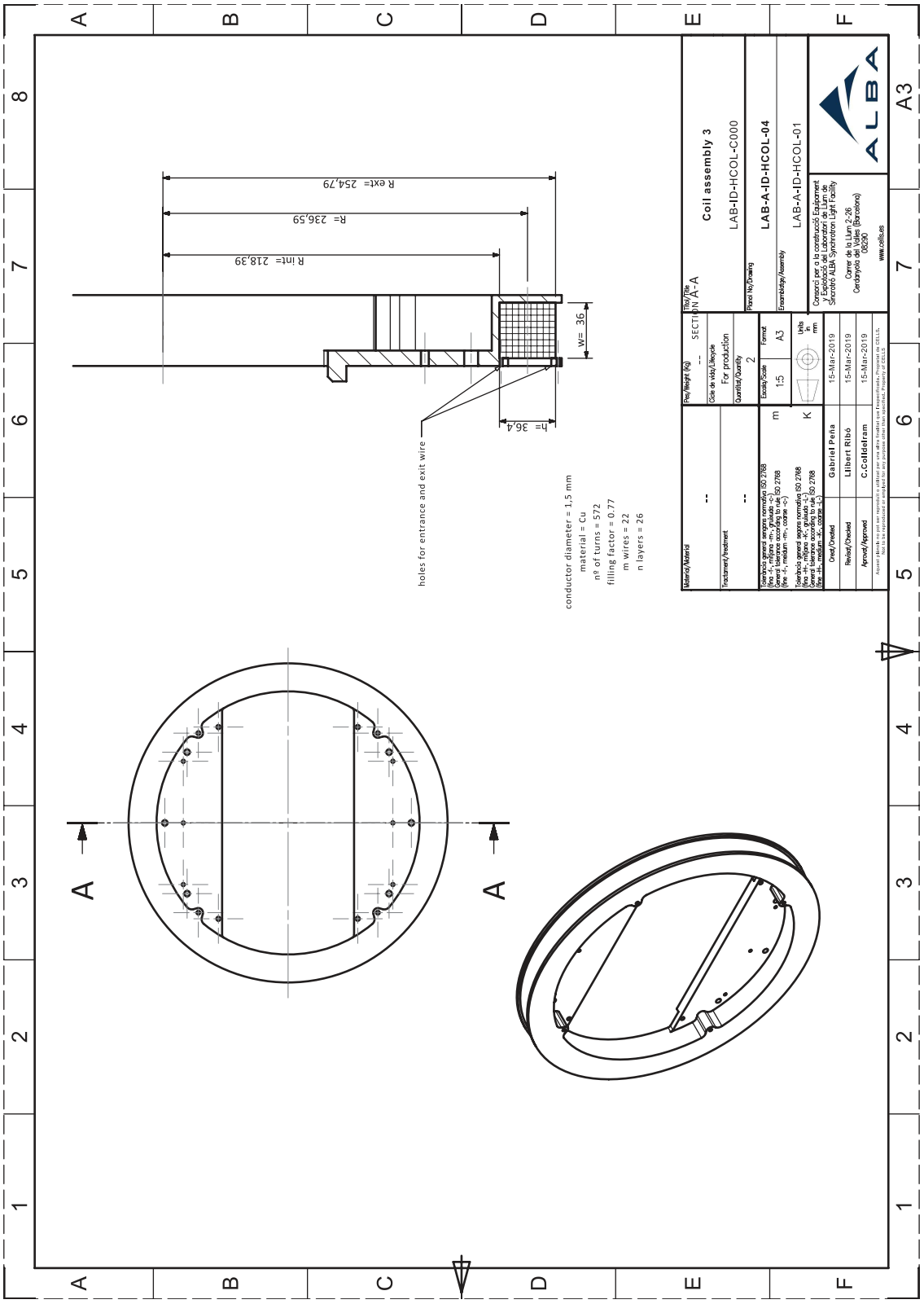
R ext= 254,79
R= 236,59
R int= 218,39
W= 36
h= 36,4
holes for entrance and exit wire
conductor diameter = 1,5 mm
material = Cu
nº of turns = 572
filling factor = 0.77
m wires = 22
n layers = 26
A
A
Coil assembly 3
LAB-ID-HCOL-C000
LAB-A-ID-HCOL-04
LAB-A-ID-HCOL-01
SECTION A-A
For production
2
A3
1:5
Gabriel Peña
Llibert Ribó
C.Colldeiram
15-Mar-2019
ALBA
A3

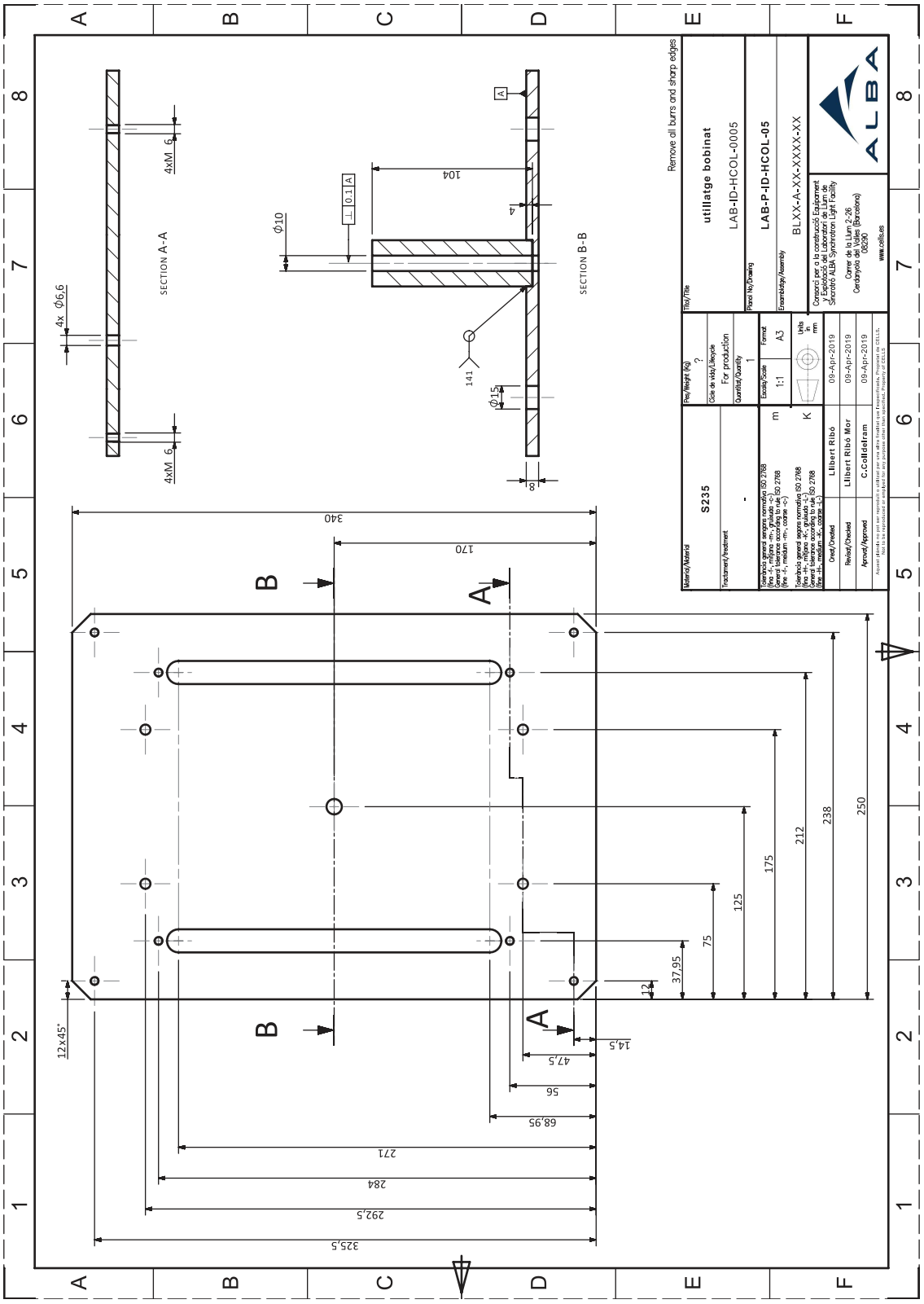
SECTION A-A
SECTION B-B
4xM 6
4x Φ6,6
Φ10
104
4
141
Φ15
8
340
170
325,5
292,5
284
271
68,95
56
47,5
14,5
12x45°
12
37,95
75
125
175
212
238
250
Remove all burns and sharp edges
utillatge bobinat
LAB-ID-HCOL-0005
LAB-P-ID-HCOL-05
BLXX-A-XX-XXXX-XX
S235
For production
1
1:1
A3
09-Apr-2019
Llibert Ribó
Llibert Ribó Mor
C.Collderam
ALBA
www.cells.es

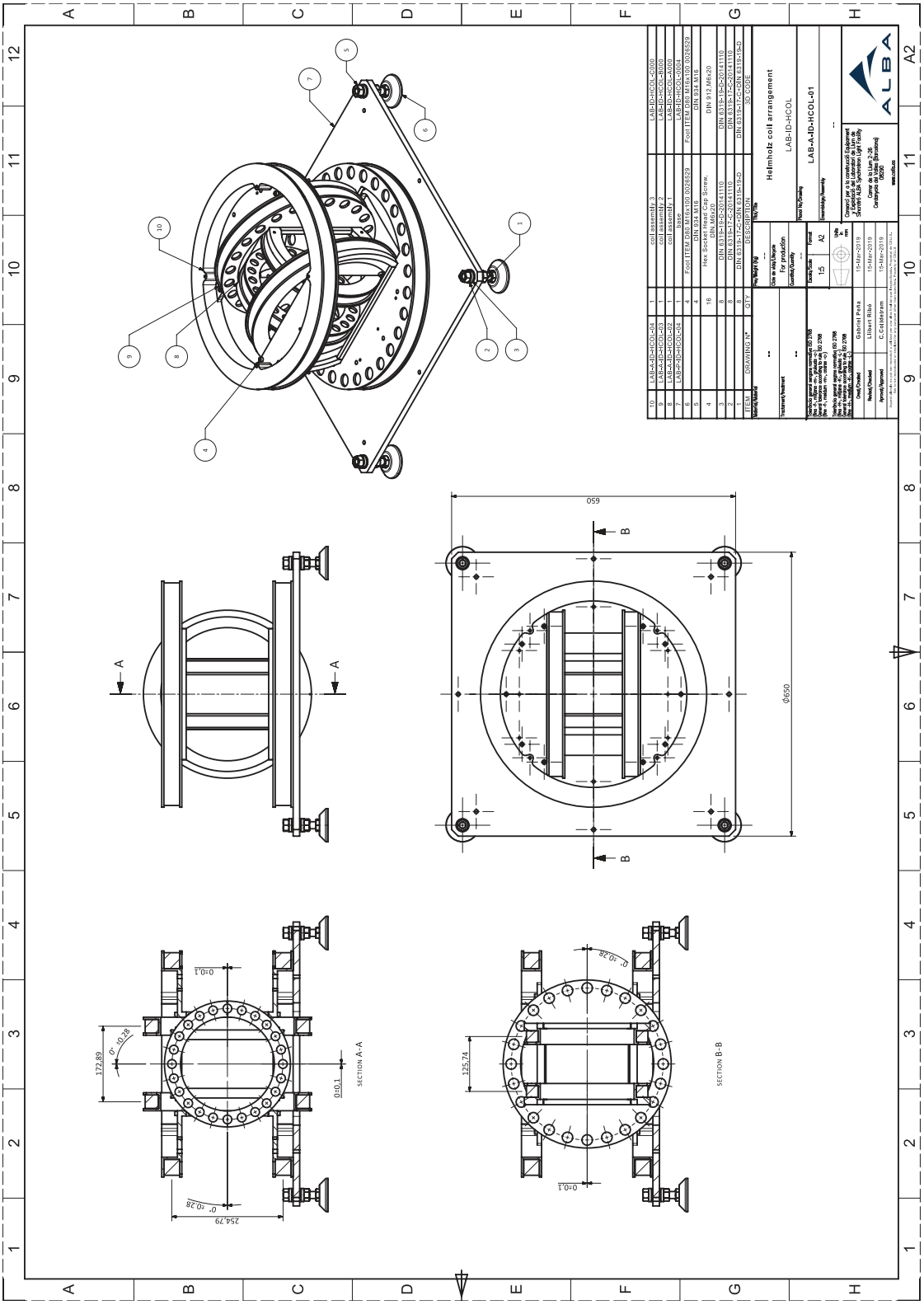
Helmholz coil arrangement
LAB-ID-HCOL
LAB-A-ID-HCOL-01
ALBA
SECTION A-A
SECTION B-B
650
Φ650
254,79
172,89
125,74